8-9-2014

SYNTHESIS OF GRAPHITIC CARBON NANOSTRUCTURES AND USE AS ELECTROCATALYST FOR OXYGEN REDUCTION REACTION

Daniel A. Moniot
University of South Carolina

SYNTHESIS OF GRAPHITIC CARBON NANOSTRUCTURES AND USE AS ELECTROCATALYST FOR OXYGEN REDUCTION REACTION

by

Daniel A. Moniot

Bachelor of Science
Moravian College, 1994

Submitted in Partial Fulfillment of the Requirements

For the Degree of Master of Science in

Chemical Engineering

College of Engineering and Computing

University of South Carolina

2014

Accepted by:

Branko N. Popov, Director of Thesis

Prabhu Ganesan, Reader

Christopher T. Williams, Reader

John W. Weidner, Reader

Lacy Ford, Vice Provost and Dean of Graduate Studies

DEDICATION

For my wife, Julie, and to my daughter Sarah who has been waiting her whole life, this is the story of “Old Carbon”.

ACKNOWLEDGEMENTS

I would like to thank my advisor, Dr. Branko N. Popov for allowing me to work and learn in his research group. Thank you also to Dr. Prabhu Ganesan for his professional assistance, guidance, countless suggestions throughout many years of research and preparation of this thesis. My thanks go to committee members, Dr. Christopher T. Williams, and Dr. John W. Weidner for serving on my thesis committee.

Thank you also to other members of Dr. Popov's research group, Tianyuan Xie, Tae-keun Kim, and Won Suk Jung for teaching me many things, for discussions, and much assistance conducting lab experiments.

I am grateful to my wife Julie beyond what words can express for her unlimited support, love, patience, understanding and encouragement these past seven years. It is upon her shoulders that I am able to reach toward higher accomplishments and together fulfill life goals. Thank you for standing by my side, because I would not have been able to complete this work without her support.

Thank you for support from family and friends including but not limited to my Dad, Sister, Kathy, Rob, Sal, Angela, Great-Grandpa, and Great-Grandma.

"If you are resolutely determined to make a lawyer out of yourself, the thing is more than half done already."

--Abraham Lincoln

ABSTRACT

Graphitic carbon nanostructure (GCN) was synthesized by a simple procedure using cobalt(II) gluconate as a precursor and used as a catalyst support for polymer electrolyte membrane (PEM) fuel cell cathode. A novel stabilization procedure was developed to enhance the thermal stability of the GCN support. Support stabilization resulted in well-defined crystalline graphitic hollow structures as confirmed by high-resolution transmission electron microscope (HRTEM). The prepared GCNs are used as support for depositing platinum nanoparticles (<4nm avg. Pt particle size) by modified polyol process. Rotating ring disk electrode (RRDE) and fuel cell studies were carried out to evaluate the catalyst performance. Cycling studies (0.6-1.0 V vs. RHE) performed on RRDE indicated better catalyst stability when compared to commercial Pt/C catalyst.

TABLE OF CONTENTS

LIST OF TABLES

LIST OF FIGURES

List of Abbreviations

ECSA ..... Electrochemical Surface Area

GCN ..... Graphitic Carbon Nanostructure

ORR ..... Oxygen Reduction Reaction

PEMFC ..... Polymer Electrolyte Membrane Fuel Cell

RRDE ..... Rotating Ring Disk Electrode

CHAPTER 1

INTRODUCTION

Porous carbon materials such as hollow carbon nanostructures are being investigated for their use in a wide variety of applications from batteries, capacitors, catalyst supports, fuel cell electrodes, and sensors [1]. The physical performance requirements are unique to each of these areas. Characteristics such as specific surface area, porosity, electrical conductivity, particle size, and morphology can be controlled using a template or nanocasting methods [2,3]. Crystallinity of the carbon structure is one property which plays a key role for some applications. Carbon materials used as supports for electrochemical catalysts require high electronic conductivity, accessible pore structure and porosity, and resistance to oxidation at low temperatures [4]. These properties are found in carbon with defined structures such as nanotubes, nanofibers, nanospheres, etc., which combine high degree of graphitic characteristic with surface accessible pores. Framework confined pores (both micro- and macro-) are not beneficial for the purpose of catalyst support. Carbon materials with these characteristics are produced at very high temperatures (>5000°C) using arc-discharge or thermal chemical vapor deposition [5] which makes them cost-prohibitive and difficult to make in large scales. A more facile preparation method to make structured carbon materials is carbon pyrolysis in the presence of first row transition metals (Fe, Co, Ni, Mn, etc.) which catalyze graphitization at moderate temperatures [6,7,8].

The metal particles catalyze the graphitization reaction of amorphous non-organized carbon into a more crystalline structure by a dissolution-precipitation mechanism [9]. The catalytic synthesis approach is often done by impregnating a carbon source with a metallic salt using wet-chemistry methods, followed by a second step of pyrolysis of the impregnated precursor [10,11,12]. One advantage of the present preparation method is that the nanostructured carbon materials can be synthesized using a single step utilizing a cost effective commercially available starting material. Cobalt and nickel gluconate are available on a metric ton basis with a low cost. This precursor is efficient at carbon graphitization in part because the transition metal is dispersed throughout the starting material at the molecular level, with each catalyst being uniformly surrounded by six-carbon chains, as can be seen by the molecular structure of the transition metal salt shown in Figure 1.1. This eliminates production variables associated with dispersing the carbon and transition metal with a two-step impregnation/pyrolysis preparation.

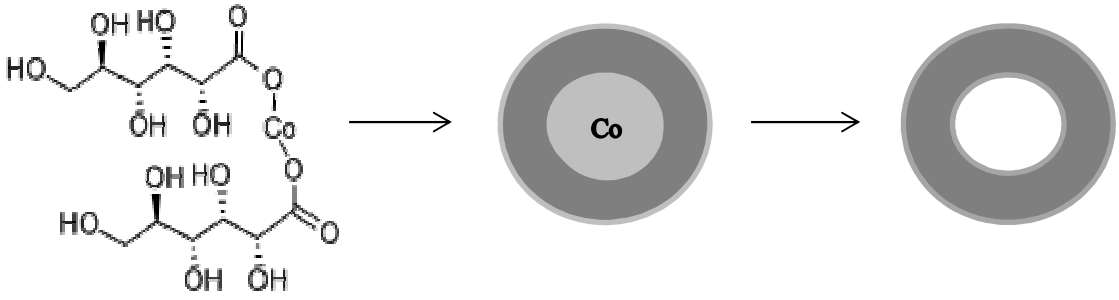

Figure 1.1 Schematic representation of GCN synthesis from cobalt gluconate.
Cobalt gluconate → Co-containing carbon structure → Graphitic carbon structure

Carbon supported catalysts used in polymer electrolyte membrane fuel cells (PEMFC) currently exhibit a significant performance decrease during durability cycling testing (0.6 – 1,0 V at 50 mV s^{-1} for 30,000 cycles). One factor contributing to this is the corrosion of carbon support on which Pt nanoparticles are deposited. The high potentials and acidic environment of PEMFC are conducive to carbon oxidation. Platinum accelerates the carbon corrosion resulting in an increase in the hydrophilic property and affects the water removal, leading to increased mass transport losses. Furthermore, carbon corrosion decreases the thickness of the catalyst layer due to Pt particle detachment from the support leading to a decrease in the electrical contact between the current collector and subsequent increase in the cell resistance [13]. Therefore, the graphitic characteristic should be more stable against this carbon loss, and the stability is further enhanced by selective removal of any remaining unstable amorphous carbon prior to platinum deposition and subsequent catalytic fuel cell use.

In the present work, we report a facile one-step synthesis procedure for preparing mesoporous graphitic carbon nanostructure from cobalt gluconate. The prepared support was used to synthesize 40% Pt/ GCN catalyst and used as a cathode catalyst support in PEM fuel cells. The synthesized support and the catalyst were subjected to variety of physical and electrochemical characterization studies.

CHAPTER 2

EXPERIMENTAL

2.1 Graphitic carbon nanostructure support synthesis

GCN support was prepared by heating cobalt gluconate powder between 800 and 1100°C under nitrogen atmosphere. Subsequent leaching in 0.5M H_2SO_4 for 2 hours at 80°C removed majority of transition metal used to catalyze the formation of graphitic structures. Carbon was stabilized by selective oxidation to remove amorphous carbon remaining in the sample from the initial pyrolysis. The resulting graphitic carbon is a hollow truncated triangle or polygon with approximate dimensions of 50 nm height and 100nm width with 10 nm wall thickness. The GCN samples are identified as GCN-t.T, where t is the pyrolysis time, and T is the pyrolysis temperature.

2.2 Pt/GCN catalyst preparation

GCN -supported Pt catalysts with 40 wt. % Pt were synthesized using a modified polyol described in previous work [14]. In brief, 40 wt. % Pt was deposited using a modified polyol deposition at elevated pH with specific amounts of $PtCl_4$ in ethylene glycol (EG). After heating at 160°C for 3 hours in EG, pH was slowly decreased. Samples were filtered with water and dried.

2.3 Physical characterization

X-ray diffraction (XRD) of samples was characterized (Rigaku D/Max 2500 V/PC) with a Cu Ka source operated at 40 keV at a scan rate of 5° min^{-1}. The elemental composition was measured using X-ray florescence (Fischerscope XDAL). Transmission electron microscopy (TEM) images were obtained with a high-resolution Hitachi H-9500 system. Brunauer-Emmett-Teller (BET) surface area and Barrett-Joyner-Halenda (BJH) pore size distribution of the GCN were measured using Nitrogen adsorption isotherm at 77°K on a Quantchrome NOVA 2000. The cobalt amount removed during acidic leaching was analyzed by ethylenediaminetetraacetate (EDTA) titration with a xylenol orange indicator which changes from purple to yellow at endpoint. In brief, leach solution was mixed with 10mL sodium acetate (4M) and H_2O (pH = 5.80±0.05) and titrated at 90-95°C with EDTA using xylenol orange indicator. The amount of cobalt remaining in the GCN support is calculated by Co mass balance. The amount of Pt and Co wt. % in the Pt/ GCN catalyst was determined using inductively coupled plasma atomic emission spectroscopy (ICP-AES). Thermal gravimetric analysis (TGA) in air (10°C min^{-1} heating rate) measured thermal stability of carbon supports in an oxidative environment using a TA Instruments Q5000.

2.4 Electrochemical studies

2.4.1 Rotating ring disk electrode (RRDE) measurements

The RRDE experiments were performed at room temperature in a three-electrode electrochemical cell. An RRDE with a glassy carbon disk (0.247 cm^2) was employed as the working electrode. The catalyst ink was prepared by blending 5 mg of catalyst with 3 mL of isopropyl alcohol and 1mL water and 0.2 mL of a mixture of a Nafion™ solution

(5 wt. %, Alfa Aesar) and isopropyl alcohol (the volume ratio of 5% Nafion^{TM} to isopropyl alcohol was 1:19) in an ultrasonic bath. Then, 10 µL of the catalyst ink was deposited onto the glassy carbon disk, resulting in 20µg Pt cm^{-2} loading. After drying, 5 mL of a mixture of a Nafion^{TM} solution (5 wt. %, Alfa Aesar) and isopropyl alcohol (the volume ratio of 5% Nafion^{TM} to isopropyl alcohol was 1:19) was coated onto the catalyst layer to ensure better adhesion of the catalyst on the glassy-carbon substrate. The electrolyte was a 0.1M $HClO_4$ solution. A platinum mesh and an Ag/AgCl electrode (0.254 V vs. RHE) were used as the counter and reference electrodes, respectively. All potentials in this work were reported as potential relative to reference hydrogen electrode (RHE). The RRDE with the catalyst layer was fixed and then dipped in the O_2-saturated electrolyte. The air bubble initially formed on the catalyst layer was removed by low-potential cycling. Then the ORR polarization curve was recorded by scanning the disk potential from 1.10 to 0.05 V vs. RHE at a rate of 5 mV s^{-1}. In order to estimate the double-layer capacitance, the electrolyte was de-aerated by bubbling with Nitrogen, and linear sweep voltammogram (LSV) was recorded at the same above-mentioned conditions. Electrochemical active surface area (ECSA) was measured by CV between 0.05 and 1.10 V vs RHE at a sweep rate of 50 mV s^{-1} using a glassy carbon rotating ring disk electrode (RRDE) in N_2 purged electrolyte.

2.4.2 Performance tests of membrane-electrode assemblies (MEAs)

The cathode catalyst ink was prepared by ultrasonically blending the catalyst with a Nafion^{TM} solution (5 wt. %, Alfa Aesar) and isopropyl alcohol. The catalyst ink was sprayed onto a Nafion^{TM} 212 membrane until the desired catalyst loading of 0.15 mg Pt cm^{-2} was achieved. The weight percentages of Nafion^{TM}: catalyst and in the dried

cathode layer and anode layer were 20 wt. % and 30 wt. % respectively. The anode catalyst for all fuel cell test was 46 wt.% Pt/C commercial catalyst (TKK TEC10E50E) dispersed and sprayed onto a gas diffusion layer (GDL) (10 BC, Sigracet Ion Power) with a Pt loading of 0.09-0.10 mg cm^{-2}. The anode and cathode were hot-pressed with another GDL for 3 min at 284°C. The geometric area of the MEA was 25 cm^2. The MEA test for H_2-O_2 was carried out in a single cell with serpentine flow channels (25 cm^2 Cell Hardware Assembly, Fuel Cell Technologies Inc.). The H_2-O_2 polarization curves were obtained using pure H_2 gas, humidified at 80°C, and pure O_2, humidified at 80°C, supplied to the anode and the cathode, respectively. The flow rates of H_2 and O_2 were 750 and 750 mL min^{-1}, respectively. Polarization experiments were conducted to measure ECSA using 100%RH H_2 and N_2 gas, with flow rates 200 and 75 mL min^{-1} respectively with no backpressure. The catalyst mass activity was measured under H_2 and O_2 (2/9.5 stoic.) with backpressure of 150kPa_{abs} and relative humidity (RH) of 100%. Pure H_2 gas, 40%RH humidified at 59°C, and Air Blend (21% O_2/79% N_2), 40%RH humidified at 59°C was supplied to the MEA at 80°C to obtain H_2-Air polarization curves. H_2 : Air supplied with stoichiometric ratio 1.5 : 1.8 with minimum flow rates of 50 and 150 mL min^{-1} respectively with backpressure of 150kPa_{abs}.

2.5 Catalyst Stability

The stability of Pt/ GCN and commercial Pt/C catalysts were evaluated in a three-electrode cell using RRDE. These catalysts were subjected to a potential cycling to 30,000 cycles between 0.6 and 1.0 V vs. RHE in an RRDE. The ORR and ECSA of the catalysts were measured periodically as described in section 2.4.1

CHAPTER 3

RESULTS AND DISCUSSION

3.1 X-ray diffraction measurements

XRD spectra is of cobalt gluconate precursor (1), after initial pyrolysis at 1000°C (2), Co peak intensity is decreased after leaching excess Co from GCN (3) and final prepared GCN after stabilization to remove amorphous carbon (4) are shown in Figure 3.1. Sharp diffraction peak at 26° representing shows a high degree of crystalline graphite structure [15]. Cobalt nanocrystals are detected between 40°-50° in XRD pattern after the initial heat treatment, and these are removed during acidic leaching to remove excess surface cobalt. Diffraction peaks for α-Co are in the pyrolyzed but unleached GCN1000 at 44, 52, and 76° representing the (1 1 1), (2 0 0), and (2 2 0) planes. Diffraction peaks at 43, 54, and 78° representing the (1 0 0), (0 0 4), and (1 1 0) planes of the graphitic structure [16] are identified in the final stabilized GCN XRD pattern in Figure 3.1. Figure 3.2 shows XRD spectra of GCN after 40wt. % Pt deposition with an additional diffraction peak attributed to the graphitic (0 0 2) crystalline plane at $2\Theta = 26°$ compared with commercial TKK 46wt. % catalyst [17]. Both spectra show the characteristic diffraction peaks of the Pt fcc structure at 2Θ = 40, 46, 67, and 81° associated with the (1 1 1), (2 0 0), (2 2 0), and (3 1 1) planes respectively.

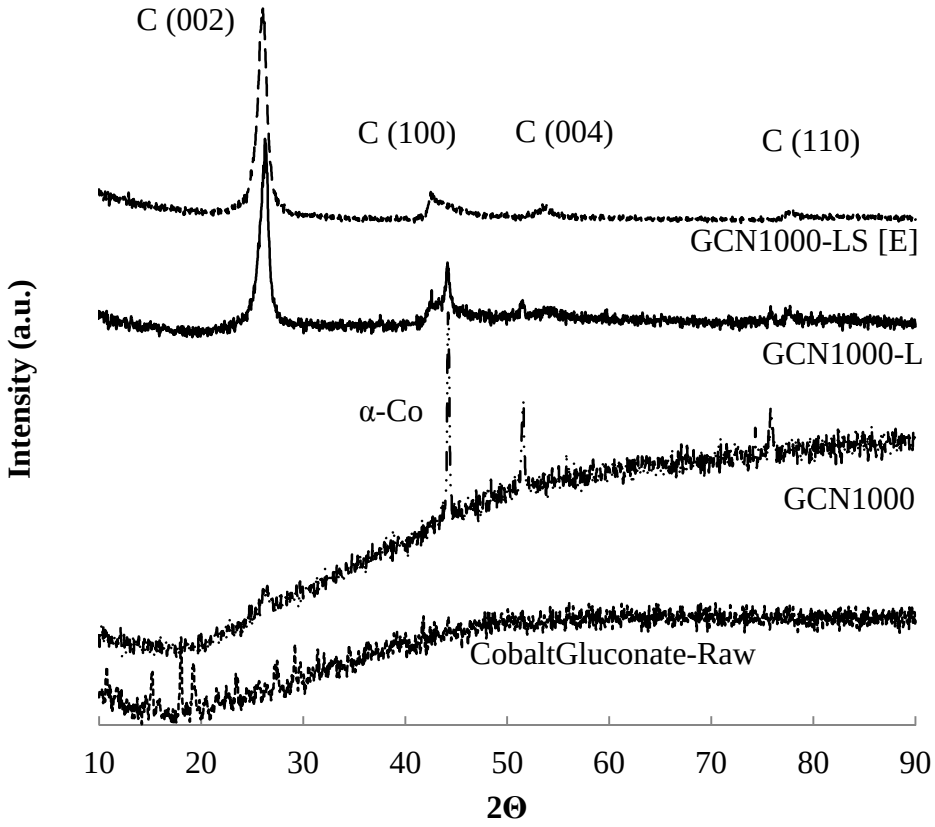

Figure 3.1 XRD pattern of GCN supports

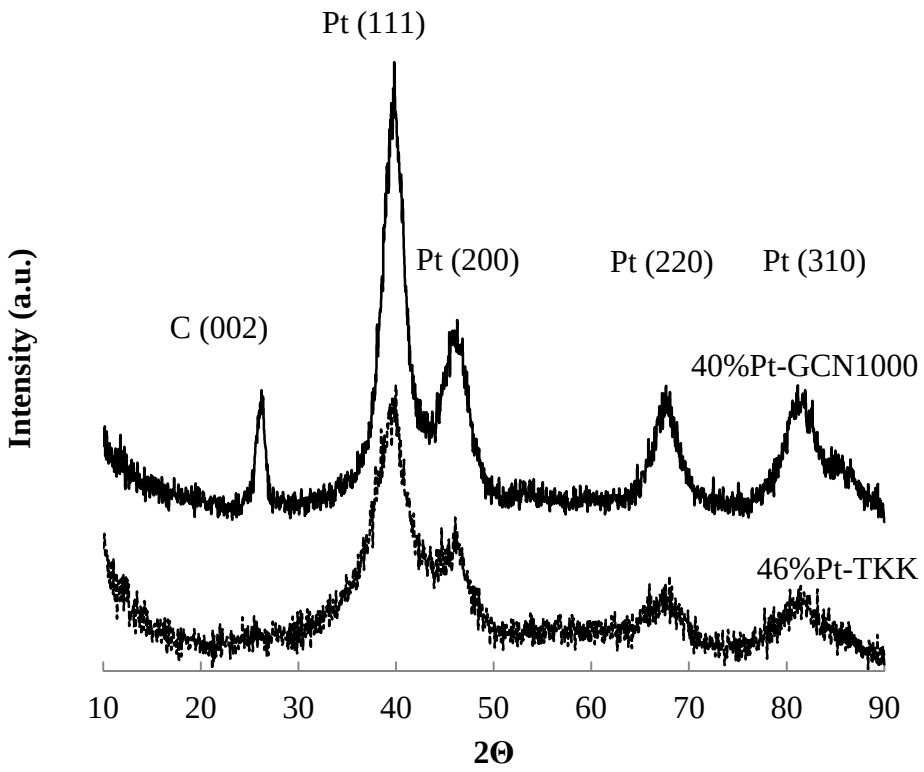

Figure 3.2 XRD of Pt/GCN1000 catalyst after Pt deposition compared with TKK commercial catalyst

3.2 Effect of heat treatment

Structural properties of the graphitic carbon nanostructures change with different heating conditions. Heating cobalt gluconate powder at temperatures >750°C produces increasingly defined graphitic structures [18]. This can be seen in TEM images of samples heated between 800-1000°C prior to stabilization (images not shown). Weight loss greater than 60% occurs during initial pyrolysis due to the fact that 12 moles of H_2O are liberated per mole of cobalt gluconate. Cobalt ions are reduced to small metallic nanoparticles dispersed throughout the gluconate pre-cursor during heating as some carbon is oxidized to CO_2. These act as nuclei which catalyze the formation of graphitic carbon layers from amorphous carbon close to the Co nanoparticle. Graphitic structures continue to grow thicker around Co nuclei according to a dissolution-precipitation mechanism using nearby amorphous carbon [6,9,19]. Glucose heated under inert atmosphere to 1000°C in absence of cobalt shows no graphitic carbon crystalline peaks by XRD, and no evidence of mesoporous porosity is detected by BET. This is confirmation that the presence of cobalt (or similar transition metal) is key to catalyze the graphitization under these moderate temperatures. Inert atmosphere pyrolysis yields porous graphitic carbon nanostructures with cobalt metal cores mixed with amorphous carbon. Iron(II) gluconate can also be used similarly, and resulting structures are long hollow carbon nanotubes instead of closed capsules [20]. Cobalt based GCNs are selected for this work, because the closed capsule structure is expected to be more stable and uniform compared with nanotubes which contain open ends that are more susceptible to oxidative attack.

After pyrolysis, excess cobalt present in the GCN support is leached out at 80°C in a measured amount of 0.5M H_2SO_4. The sample is filtered, washed and dried. Cobalt amount removed during acidic leaching was quantified by EDTA titration of the filtrate with a xylenol orange indicator. Mass balance of cobalt accounting for weight loss during initial heating and leaching results in 5.2 wt. % cobalt present in the GCN support after leaching.

GCN-1000 with 5 hour initial heat time at 1000°C was selected as the GCN support for subsequent Pt deposition and electrocatalytic performance evaluation based on combination of highest degree of graphitization and large BET specific surface area. This combination was estimated to provide the maximum GCN-support stability with minimal mass-transport resistance for reactant gases during fuel cell testing.

3.3 Support stabilization and refinement

Stabilization of the carbon is done prior to Pt deposition by eliminating amorphous carbon impurities. Stabilization of the GCN support is beneficial against both physical corrosion as well as electrochemical effects. The corrosive effects of the fuel cell environment should disproportionally affect amorphous carbon more because it has a higher specific surface area than graphitic carbon structures. This is similar to the Ostwald ripening effect which causes smaller Pt nanoparticles to dissolve and redeposit onto larger existing Pt particles. Amorphous carbon impurities in carbon nanotubes have been reported to have a strong negative impact on electrochemical performance as measured by cyclic voltammetry [21]. Removal of amorphous carbon prior to deposition of Pt catalyst is expected to result in enhanced physical and electrochemical stability.

Table 3.1 Graphitic carbon nanostructures prepared at different initial pyrolysis conditions show similar BET surface area.

Sample	HT Temp	HT time	Stabilization	Surface Area $m^2 g^{-1}$
GCN	1000	1Hr	Condition E	132
GCN	1000	5Hr	Condition E	151
GCN	900	3Hr	Condition E	145
GCN	850	3Hr	Condition E	158
GCN	800	1Hr	Condition E	150
GCN	1000	5Hr	None	153
GCN	1000	1Hr	None	177
GCN	800	1Hr	None	186

Yields: HT#1 35 wt. %; Stabilization 83 %; Overall yield 17wt. %

Graphitic carbon can be oxidized at slower reaction rate relative to amorphous carbon [22]. Graphitic carbon is thermodynamically more stable than single bonded carbon, as is discussed in section 3.5. Acidic $KMnO_4$ has been reported as effective for selective removal of amorphous carbon from graphitic carbon structures [20,22].

$$3\,C + 4\,KMnO_4 + 4\,H^+ \rightarrow 4\,MnO_2 + 3\,CO_2 + 4\,K^+ + 2\,H_2O$$

Residual MnO_2 removal was found to be difficult for these synthesized GCN structures even after strong acidic leaching, and additionally $KMnO_4$ oxidation reaction is also temperature dependent, resulting in complete oxidation at 100°C, and low yields at reduced temperatures. In order to evaluate the performance of the GCN-support without any performance contribution from MnO_2, a different method of selective oxidation which would not leave transition metal impurities was preferred.

Alternate pathways to remove amorphous carbon were found in literature. A different stabilization method to eliminate amorphous impurities was pursued in order to avoid Mn contamination effects in the GCN catalyst support. A variety of different classifications has been reported for selective removal of amorphous carbon, including physical separation methods which do not require carbon oxidation such as centrifugation and chemical oxidation via gas phase or liquid phase methodologies [23]. H_2SO_4/HNO_3 (3:1, v/v) at 70-120°C, is used to partially oxidize carbon nanotubes [24] and can be followed by aqueous NaOH treatment to remove residual debris from graphitic surfaces after oxidation [25]. Gas phase oxidation using reactants such as O_2, air, or HCl is another reaction pathway for amorphous carbon elimination [26,27]. Polyoxometalates such as phosphotungstic acid has been used followed by centrifugation to remove

impurities and solubilize carbon nanotubes with high yields [28]. Nitric acid baths at various reaction times and temperatures are one of the most commonly applied approaches used for removal of metallic and amorphous carbonaceous impurities [29]. The resulting oxidation effect is dependent on both nitric acid concentration and reaction time [30], and fluid temperature also affects the strength or rate of oxidation as was seen with the initial permanganate results above. Acid solutions of various compositions and concentrations have also been reported for surface functionalization without destruction of single wall – and multiwall carbon nanotubes (SWCNT, MWCNT) with oxygen moieties. It is thus possible to remove a majority of undesired amorphous carbon while retaining the beneficial graphitic nanostructures.

It is important to remove the transition metal used as catalyst for graphitization prior to stabilization for optimal results, for both methods. Presence of transition metal catalyzes the oxidation reaction. This decreases the temperature or solution strength where reaction will be selective. This can result in complete oxidation of all carbon. Oxidizing carbon based samples containing 21 wt.% Cobalt results in a 71.3±1.1 wt.% loss, compared with similar carbon based support with <1 wt.% Cobalt yielding 34.5±3.6 wt.% loss under same condition. A specific stabilization condition must be found for any support which contains metals such as Pt or first row transition metals which can act to catalyze oxidation reaction to occur under milder conditions.

Stabilization is done by selective separation or oxidation of amorphous vs. graphitic carbon. Surface area and support properties can be controlled and altered by adjusting strength and duration of the selective-oxidation reaction. Excessive oxidation will consume the desired GCN structures in addition to the amorphous carbon, so a

balance may need to be achieved among graphitic purity, electrocatalytic performance, yield and physical characteristics such as porosity, conductivity, surface area, hydrophobicity. By removing unstable amorphous carbon prior to Pt deposition, Pt will only be supported by more thermodynamically stable crystalline graphitic carbon structures. This should improve catalyst durability during electrochemical cycling

After preparing a maximum stability GCN-support sample for Pt Deposition with long initial heating time to maximize graphitic character and with most aggressive oxidation condition to ensure complete removal of all amorphous carbon, milder process conditions were investigated to optimize stabilization wt.% yield, specific surface area, and evaluate porosity effect on the GCN-support.

GCN graphitization degree which is controlled by initial cobalt gluconate pyrolysis time and temperature improved wt.% yield by 1 – 2% seen in Figure 3.3 with the difference between GCN prepared with 1 and 5 hour pyrolysis times at 1000°C representing moderate and high graphitization respectively. Using milder oxidation conditions, by decreasing the oxidation fluid temperature by 35°C, stabilization yield increased from 83 wt. % to 91% for the same reaction time. Figure 3.4 shows the decrease in temperature has a more significant impact on yield improvement with longer selective-oxidation reaction times.

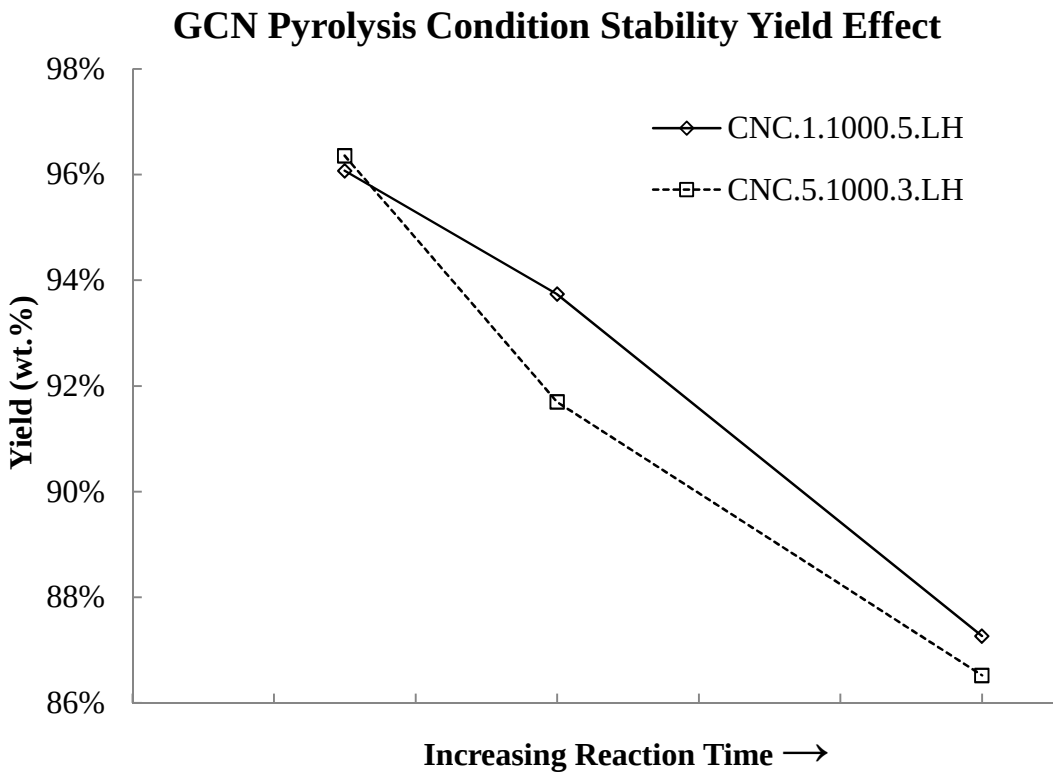

Figure 3.3 Degree of graphitization represented by length of cobalt gluconate initial pyrolysis time has small 1% - 2% impact on stabilization wt. % yield.

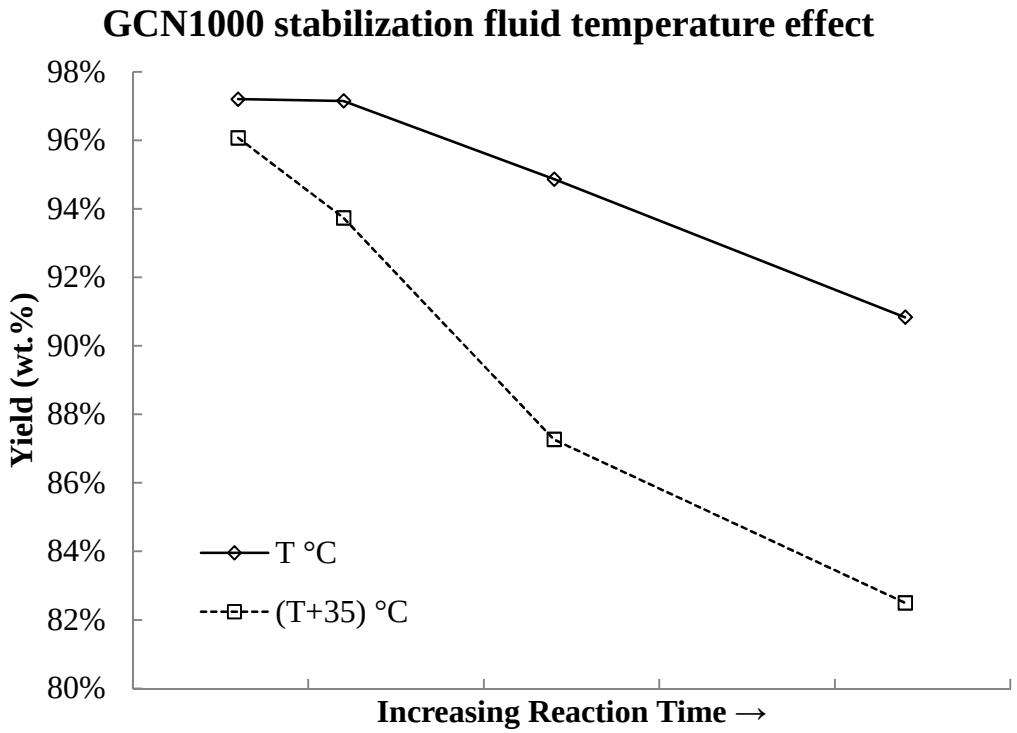

Figure 3.4 GCN-Support stability yield increased with use of reduced oxidizing temperature

3.4 Adsorption characteristics

N_2 adsorption isotherm having a broad adsorption– desorption hysteresis loop, characteristic of mesoporous materials with cage-like pores [31] displays similar curve shape and gas absorbance in Figure 3.5 for GCN supports with moderate and high graphitization. A clear hysteresis at relative pressure ratios >0.4 indicates the presence of mesoporous structure, and the upward curvature shape seen in the hysteresis between adsorption and desorption suggests a cylindrical pore shape. Jansen reported the peak pore diameter near 4nm is an artifact of the BJH-method and could represent pores with constricted openings of pore sizes up to 4nm. At a relative pressure of ca. 0.45 there is a sudden desorption of nitrogen, which is visible as the closing of the hysteresis loop at this pressure. All inkbottle type micropores or mesopores with pore necks smaller than 4 nm will release their nitrogen at a relative pressure of ca. 0.45 [32]. In Figure 3.6 the pore size distribution is given as analyzed using the BJH-method of the adsorption isotherm, and average values are summarized in Table 3.2.

Treating GCN's with longer selective oxidation times in conditions B, C, D and E respectively shows the pore structure progression toward larger pore dimensions from initial unoxidized condition A before stabilization. This progression can be seen for highly graphitized GCN.5.1000 (5Hr pyrolysis) in Figure 3.7 stabilized at temperature (T+35)°C; for GCN.1.1000 (1 Hr pyrolysis) in Figure 3.8 stabilized at temperature (T+35)°C; and for the same GCN.1.1000 support stabilized at reduced temperature (T)°C in Figure 3.9.

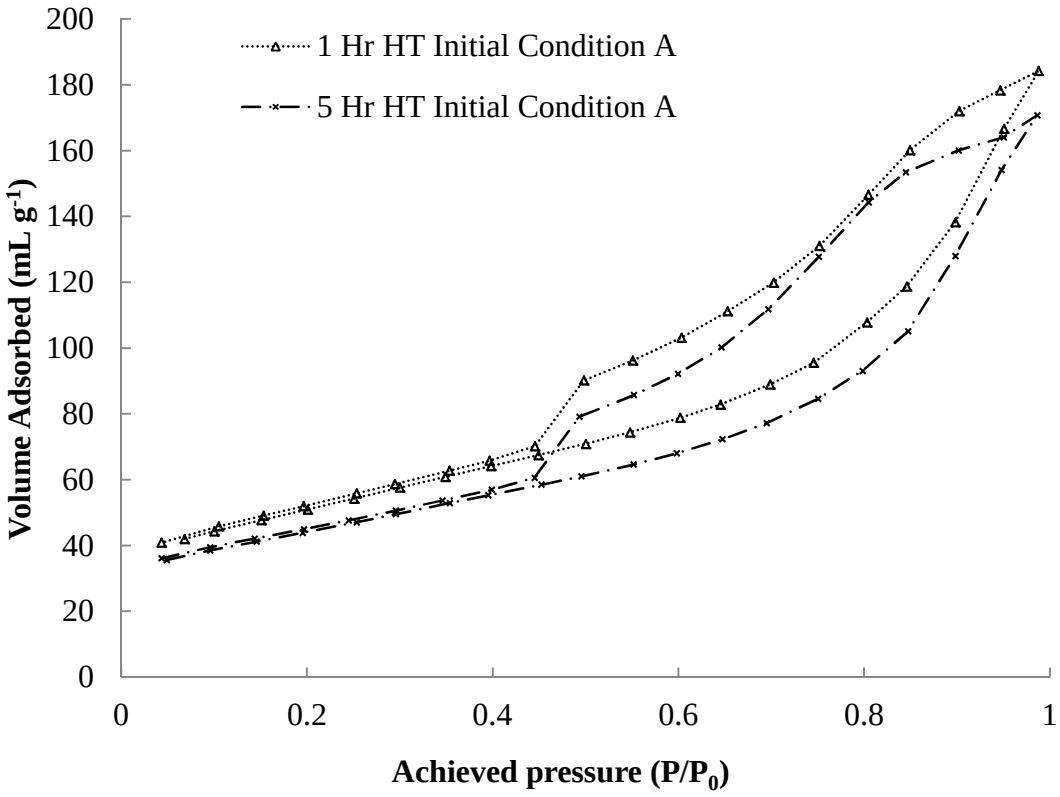

Figure 3.5 N_2- adsorption isotherms of GCN supports before stabilization.

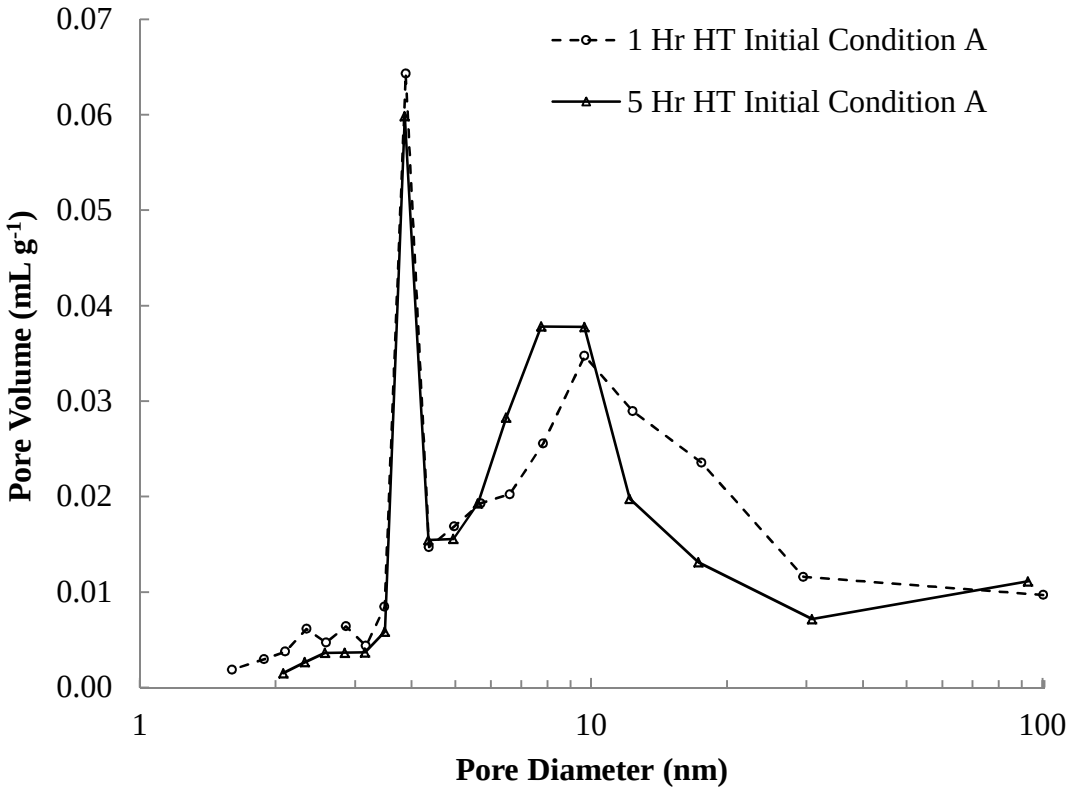

Figure 3.6 Mesoporous GCN pore size distribution (BJH method) before stabilization.

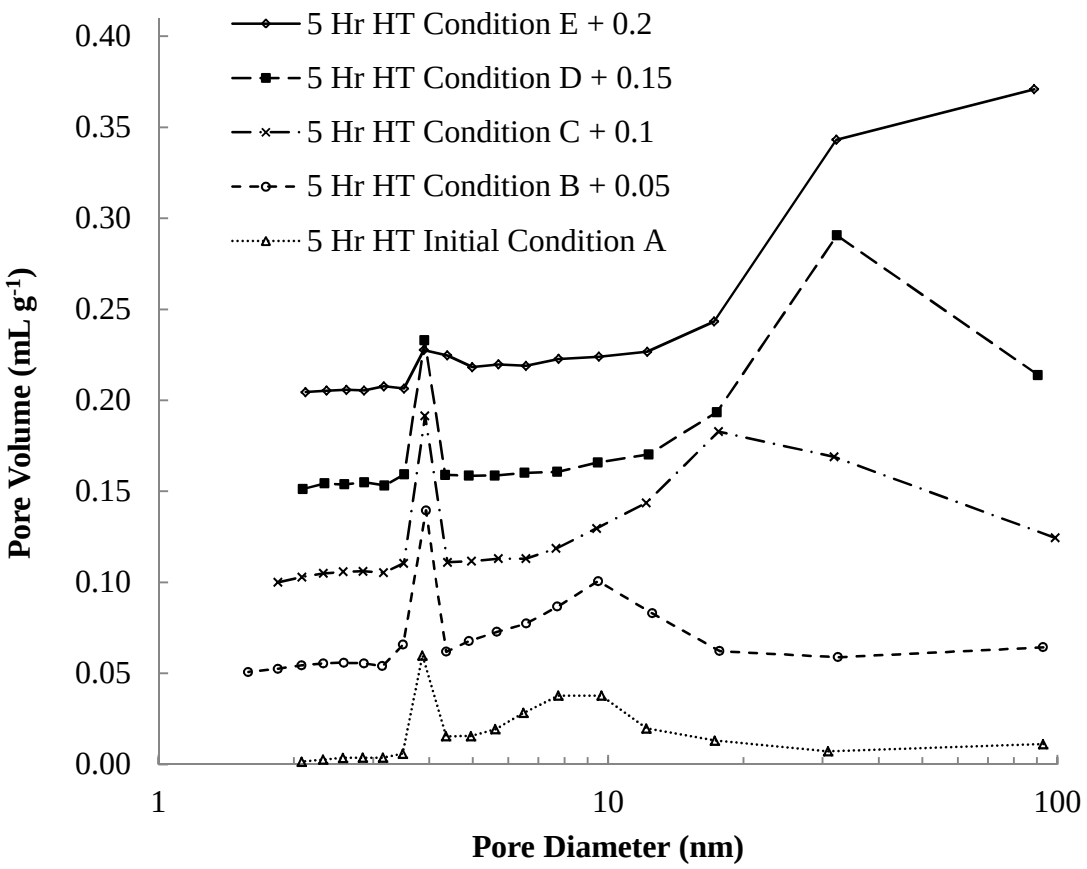

Figure 3.7 Pore size distribution of highly graphitized GCN support with increasing stabilization times from initial Condition A < B < C < D < E. Stabilization temperature (T+35) °C.

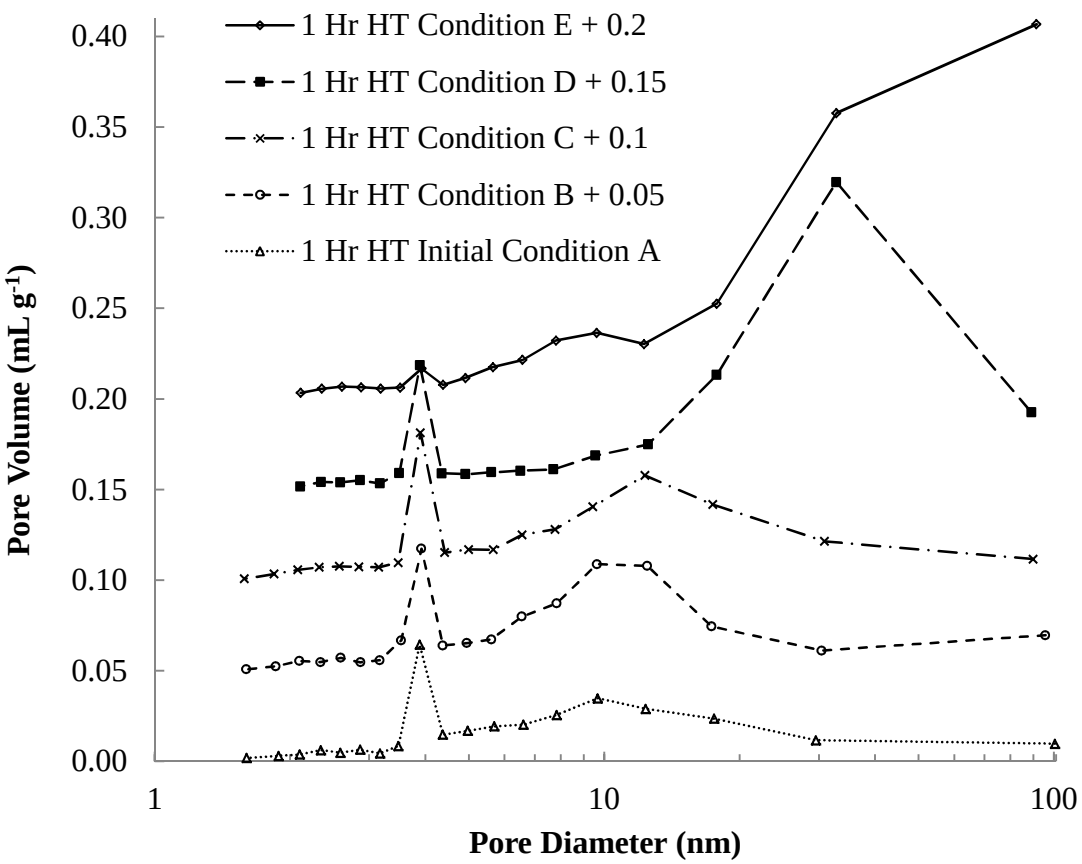

Figure 3.8 Pore size distribution of moderately graphitized GCN support with increasing stabilization times from initial Condition A < B < C < D < E. Stabilization temperature (T+35) °C.

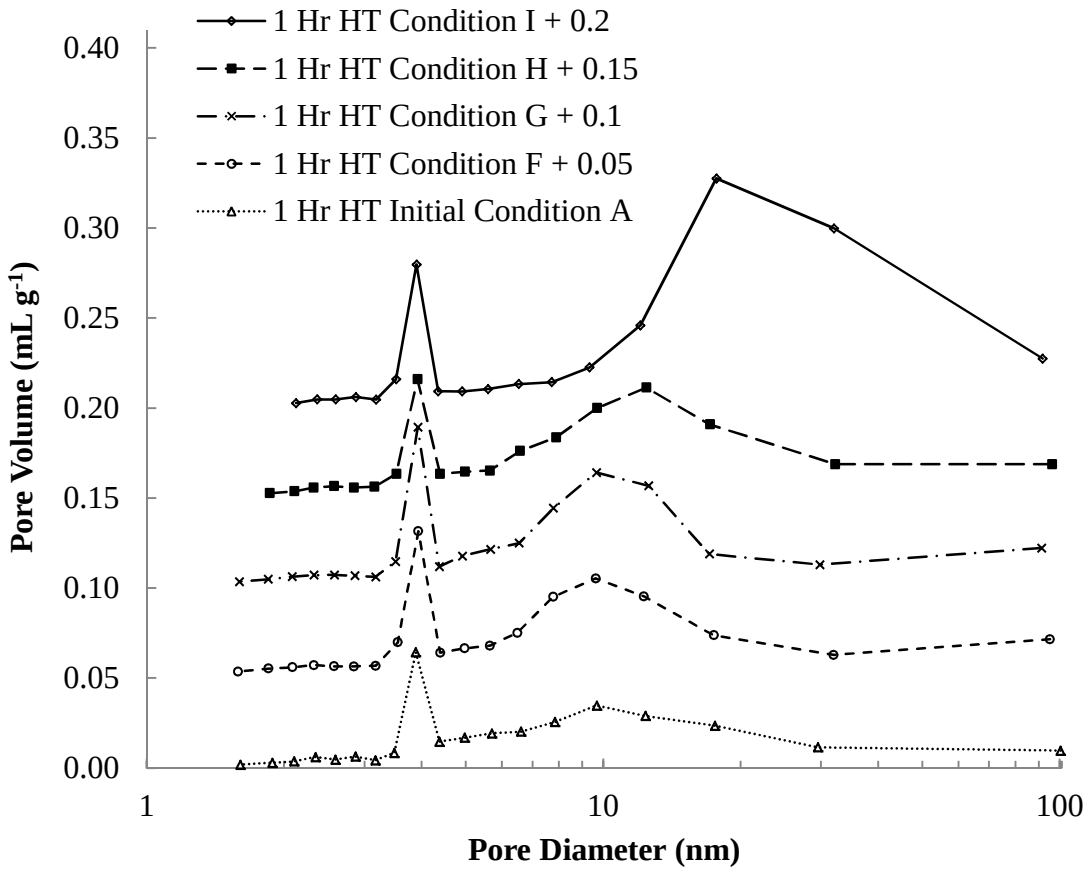

Figure 3.9 Pore size distribution of moderately graphitized GCN support with increasing stabilization times from initial Condition A < B < C < D < E. Reduced stabilization temperature (T) °C.

Porosity increases for pore distributions near 4 and 10nm diameter under mild oxidation condition B. It can be inferred from the adsorption data that a majority of inkbottle type pores are unclogged by mild oxidation B, seen by the porosity change at 4nm from A to B. Pore diameter for condition B remains almost unchanged with increased pore volume, as amorphous carbon is preferentially oxidized and removed from pores in the support. The volume of gas adsorbed shows a corresponding increase as amorphous carbon debris is cleaned out of pores, shifting more adsorption toward higher relative pressures. It is not clear if all amorphous carbon has been removed in condition B. Pores are becoming deeper as amorphous carbon is selectively oxidized without significant etching of pore walls, as the pore diameter remains largely unchanged. Stronger oxidation does not change the microporosity detected in all samples in conditions C and D, compared with condition B, as evidenced by near constant pore volume at 4 nm pore diameter as mesoporous pore dimensions continue to increase. This suggests the shell of the GCN may have inherent microporous character, or gases may be escaping from the hollow core at low pressures.

Differences between the support properties and stabilization temperature begin to differentiate as the reaction time increases. The average pore diameter size distribution increases in condition C as the pores of the GCN support increase in physical dimensions due to oxidative attack on the pore walls for samples stabilized at elevated temperature (T+35)°C. GCN.5.1000 pore size shifts larger compared to GCN.1.1000 stabilized at the same temperature. This may be due to greater degree of graphitization in the 5-hour sample. Once amorphous carbon has been consumed in GCN.5.1000, then the oxidation would no longer be selective and would start increasing size of all GCN pores and also

decreasing weight yield of the reaction. N_2 adsorption isotherm hysteresis shape shifts in condition C, to higher partial pressures, with the high graphitization sample showing a more significant change and is displayed for highly graphitized GCN.5.1000 (5Hr pyrolysis) in Figure 3.10 stabilized at temperature (T+35) °C; for GCN.1.1000 (1 Hr pyrolysis) in Figure 3.11 stabilized at temperature (T+35) °C; and for the same GCN.1.1000 support stabilized at reduced temperature (T) °C in Figure 3.12. This shape change can be due attributed to decreased effect of pore wall surface roughness with increased pore diameter [33]. There is no corresponding increase in the pore size distribution or N_2 adsorption isotherm shape of GCN.1.1000 stabilized for the same time as condition C with reduced temperature (T) referred to as condition G.

BJH Pore Size distribution shows diminished pore volume at 4nm and increased macroporous character above 50nm in GCN-5-1000 and GCN.1.1000 supports treated at temperature (T+35)°C with excessive oxidation condition E. Oxidation is consuming walls of mesoporous pores, resulting in a shift from initial mesoporous character into macroscopic pore sizes at very long reaction times. This suggests that micro- and mesoporous structure is substantially consumed during excessive oxidation of GCN-supports.

The same CNC.1.1000 support sample initially pyrolyzed 1 Hr at 1000°C shows a shift toward smaller average pore size and reduced macroscopic pore characteristic greater than 50nm by reducing oxidation fluid temperature -35°C for the same reaction times. Pore Volume as a function of increasing oxidation reaction times at reduced fluid temperature shows a pattern of increased pore volume between 5-20nm diameter with little shift in average pore size up to moderate reaction times. This can be attributed to

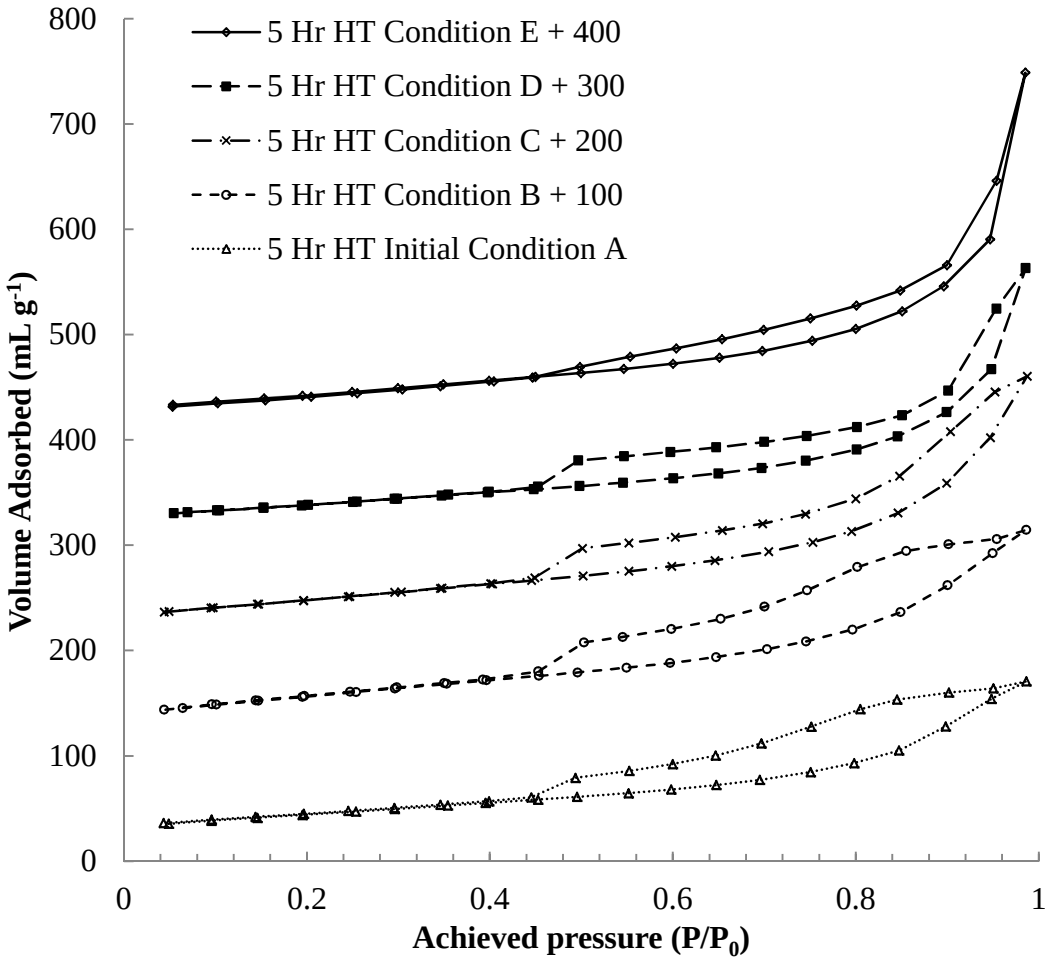

Figure 3.10 N_2 adsorption of highly graphitized GCN with increasing stabilization times from initial Condition A < B < C < D < E. Stabilization temperature (T+35) °C.

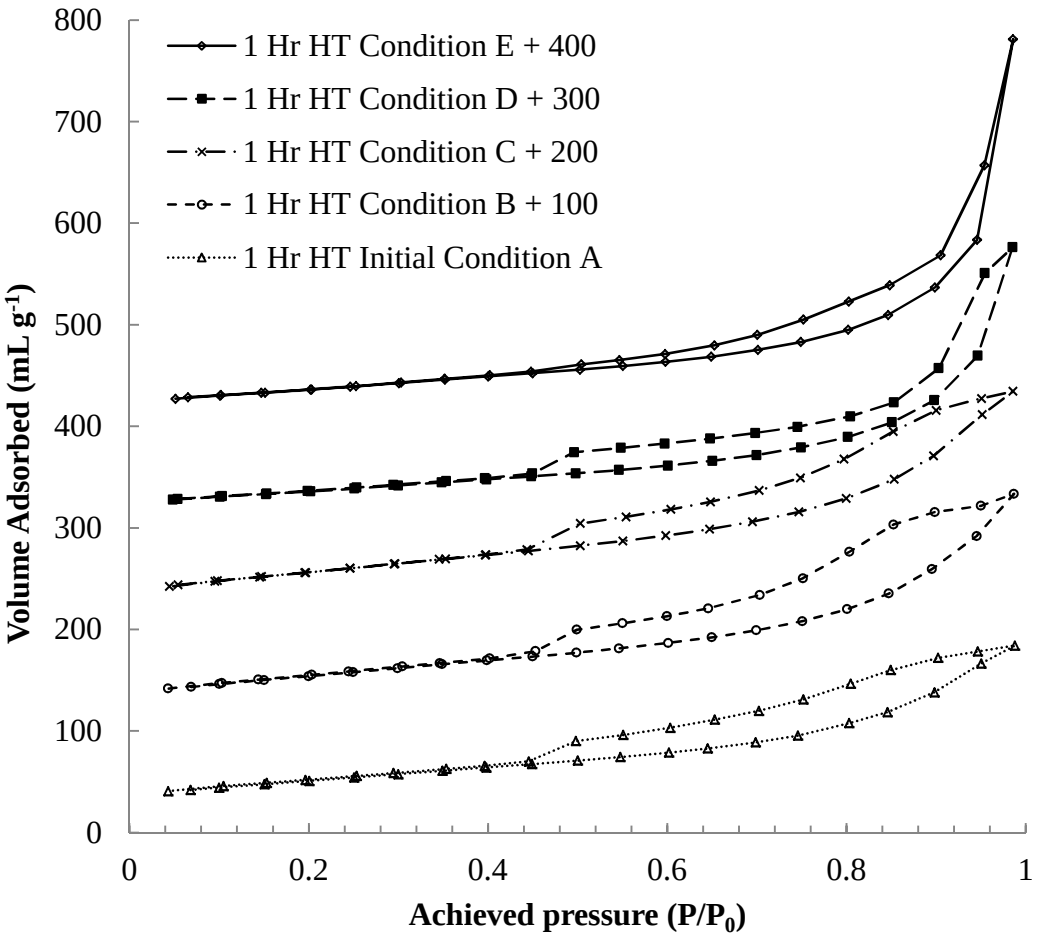

Figure 3.11 N_2 adsorption of moderately graphitized GCN during support stabilization with increasing stabilization times from initial Condition A < B < C < D < E. Stabilization temperature (T+35) °C.

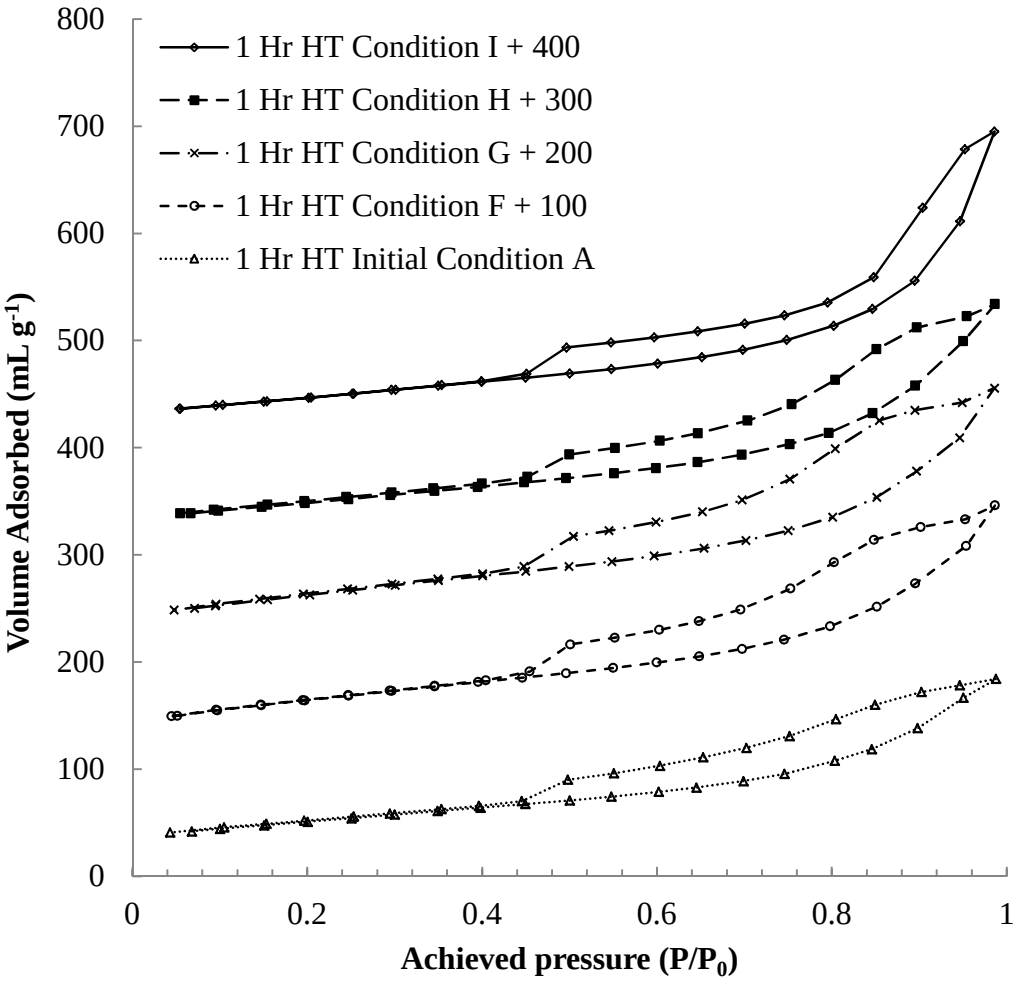

Figure 3.12 N_2 adsorption of moderately graphitized GCN with increasing stabilization times from initial Condition A < B < C < D < E. Reduced stabilization temperature (T) °C.

selective oxidation of amorphous carbon, unclogging existing pores. The very small change in adsorption isotherm hysteresis shape also suggests that deeper pores increase pore volume without corresponding average pore diameter increase. Increasing reaction times show an increase in the average pore diameter as the selective oxidation reaction proceeds to longer conditions H and I.

Pore Diameter begins to increase toward larger mesoporous sizes at longest oxidation reaction times as pore walls are etched, making more GCN-support pores surface accessible, as seen by adsorption isotherm shape change and increased volume at relative pressures above 0.8. Average pore size and BET surface areas trends are compared in Figures 3.13 and 3.14 for the various stabilization and support conditions.

Condition E represents excessively aggressive oxidation to assure that all amorphous carbon has been completely removed. The negative impact of excess oxidation is the removal of beneficial pore structure on the GCN surface, shifting some pores from mesoporous to larger macroporous classification and reduced weight yield for condition E vs. all other samples. Final Surface area 151 $m^2 g^{-1}$ was measured using BET for GCN.5.1000 with 1000°C initial pyrolysis temperature, and Table 3.1 shows the as prepared BET surface area in the range of 132 - 158 $m^2 g^{-1}$ for GCN samples prepared at different temperatures.

N_2 adsorption isotherm shows surface accessible porosity of the graphitic carbon nanostructures after preparation, leaching and stabilization. This is evident from the large N_2 adsorption at relative P/P_0 ratios >0.8. The large adsorption at higher pressures indicates that pores are accessible for Pt deposition or gas diffusion, and TEM images in section 1.3.5 show the benefit of this pore structure, evident in the uniform deposition of

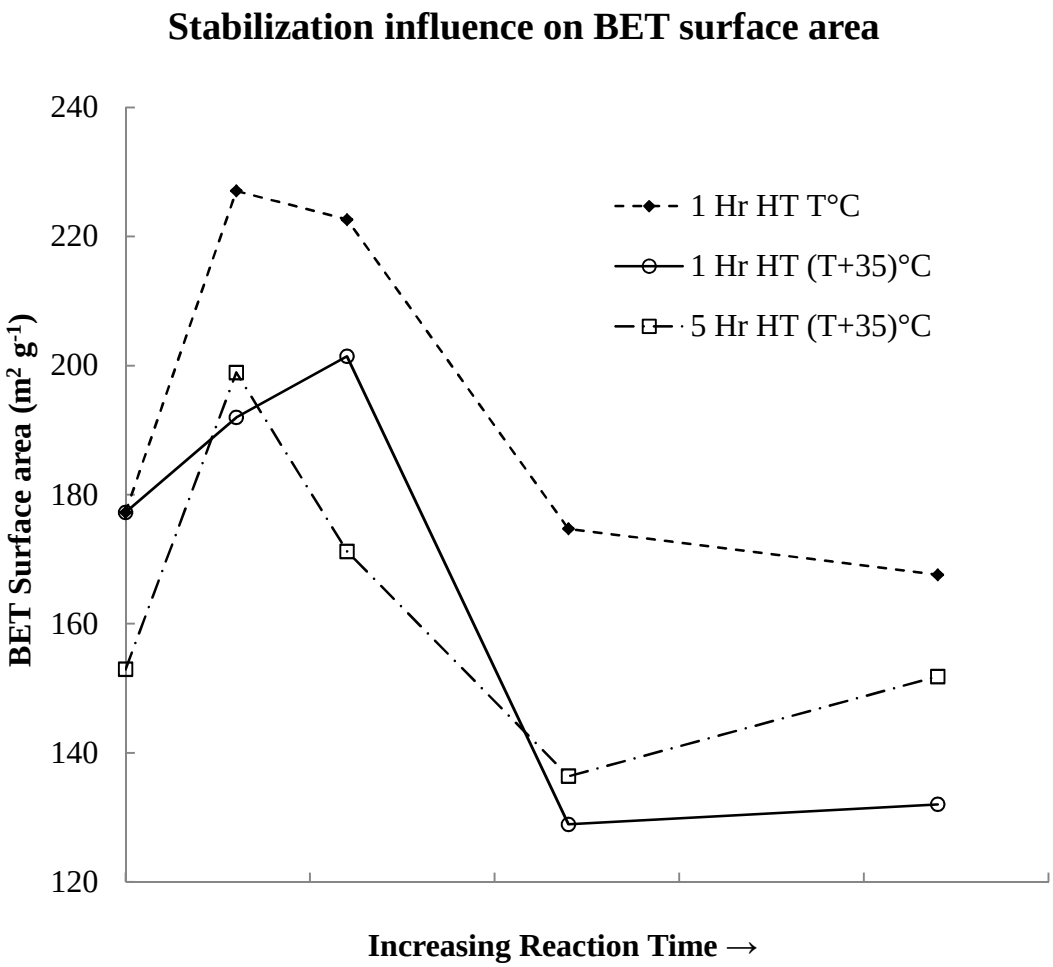

Figure 3.13 Stabilization condition influence on BET surface area

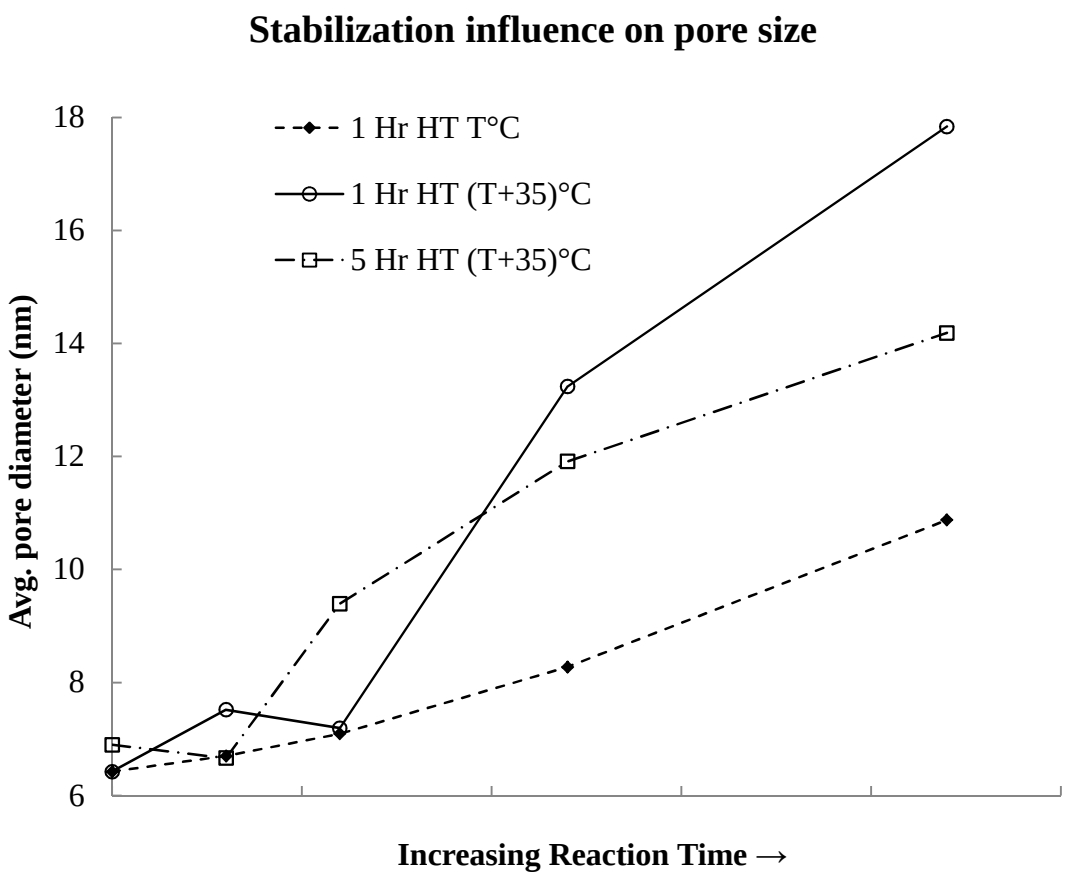

Figure 3.14 Stabilization condition influence on average pore size distribution

Table 3.2 Physical properties of GCN -support

	BET surface area ($m^2 g^{-1}$)	BJH Avg. pore diameter (nm)	Yield weight%	TGA T_{de} (°C)
Ketjenblack high surface area carbon	835	7.55	--	695
GCN1000A (no stabilization)	152	8.53	--	699
GCN1000B	223	7.10	97.2	--
GCN1000I	168	10.86	90.8	713
GCN1000E	132	17.84	83	>750

small Pt nanoparticles. This effect becomes more pronounced with stronger oxidation condition and the large adsorption in conditions C, D, and E are indication that these pores are easily surface accessible for Pt deposition or easy transport reactant gases to catalyst surface during fuel cell operation.

Porosity, wt. % yield, surface area, and graphitic purity of these graphitic carbon nanostructures can be adjusted and tuned by controlling the strength and duration of selective oxidation, and support properties. This new approach can be applied generally to other carbon based catalyst support systems by optimizing the selective oxidation reaction conditions for the particular properties of a given support system.

A mixture of graphitic structures with defined shapes and amorphous carbon after initial pyrolysis at 1000°C and acidic leaching to remove excess surface Co, are shown in Figure 3.15 with diameters ranging between 25 and 150nm. After stabilization, the highly crystalline nature and hollow triangular shape with approximate dimensions ~140nm wide by ~50nm thick is evident in Figure 3.16 having distinct crystalline faces. Wall thickness ~10-20nm thick with individual graphitic carbon layers are evident in Figure 3.16 inset. TEM pictures and dimensions are in agreement with literature reported values of 10-30nm wall thickness and 50nm diameter by M. Sevilla [20] for GCN prepared from the same cobalt gluconate precursor using a different stabilization method.

3.5 Thermal Stability of Support

Thermal gravimetric analysis was performed to evaluate the thermal stability effect of amorphous carbon removal. Experiments were performed in air to simulate oxidative attack which GCN-catalyst will be subjected to in PEM fuel cell environment. Samples were heated in air with a 10°C min^{-1} ramp rate. The increased thermal

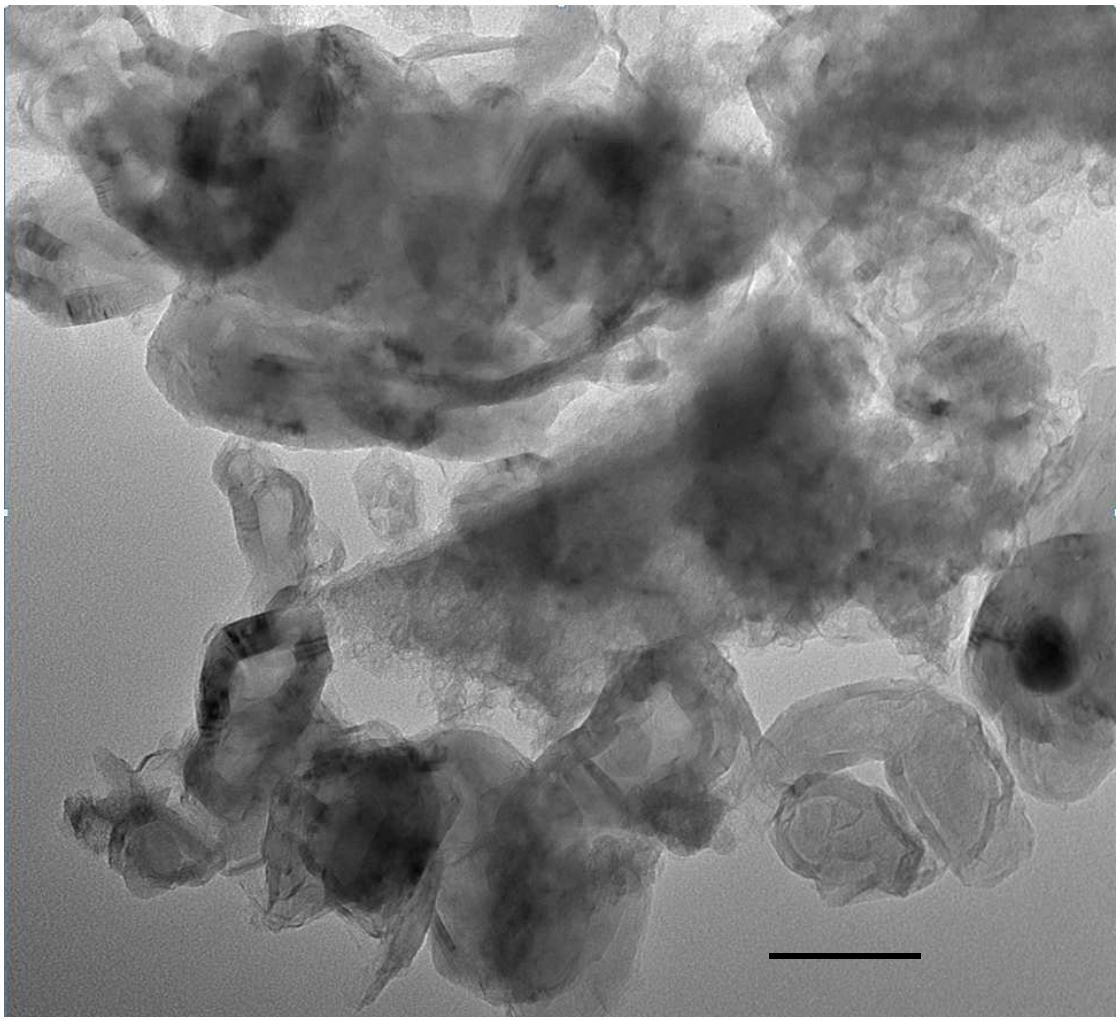

Figure 3.15 GCN1000-support after acidic leaching and before stabilization shows a mixture of defined graphitic shapes and amorphous carbon. Bar represents 100nm scale.

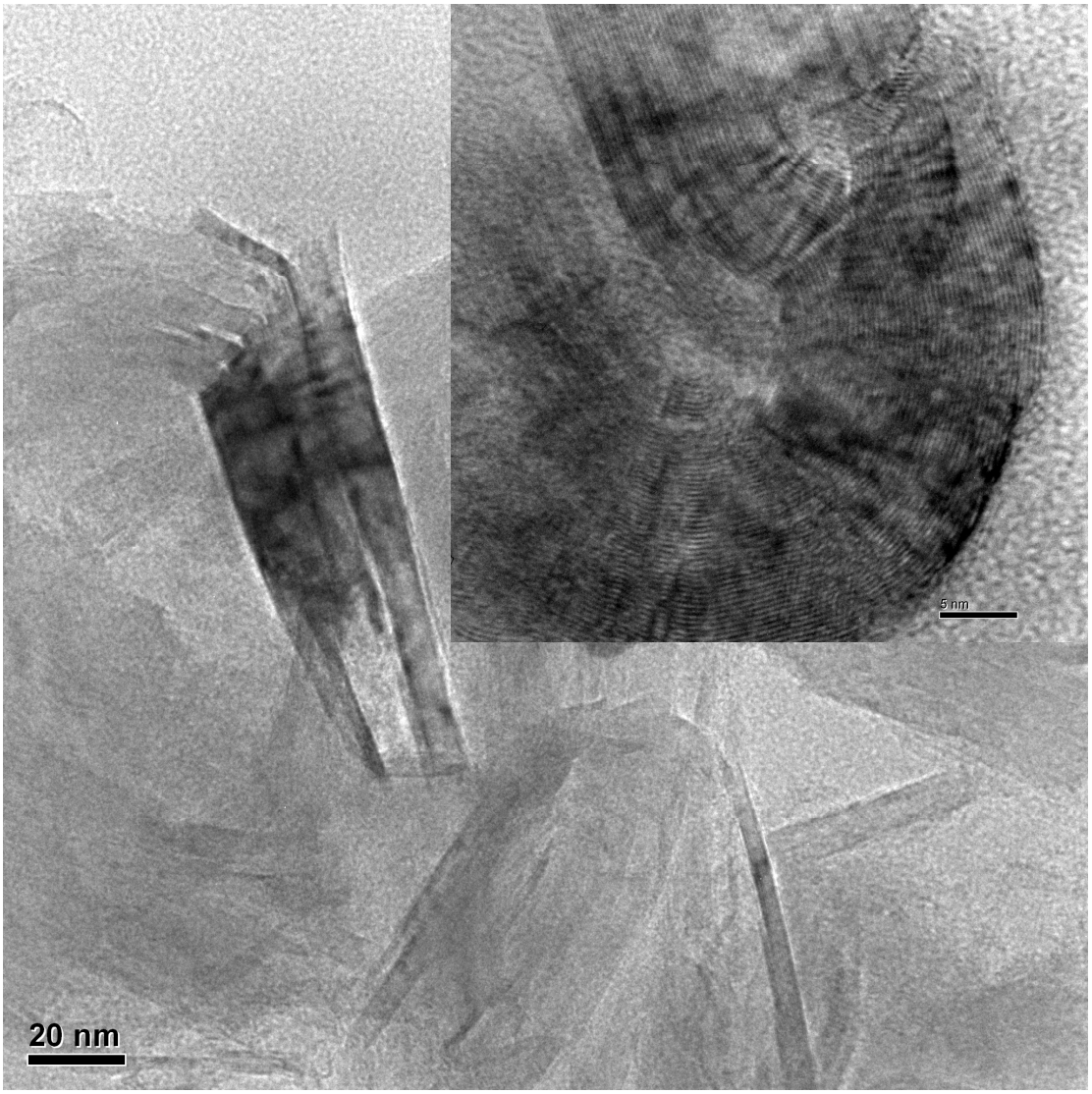

Figure 3.16 HRTEM shows a defined GCN structure with ordered layers of graphitic carbon after stabilization to remove amorphous carbon. Bar represents 20nm scale. Inset shows 10nm thick ordered graphitic wall structure of GCN. Inset bar represents 5nm scale.

decomposition temperature, T_{de}, and a small difference between 550 and 650°C, in Figure 3.17 shows the improved stability performance of stabilized GCN1.1000.LHS compared with same sample without amorphous carbon removal, which can be attributed to the oxidative loss of amorphous carbon. Samples corresponding to initial GCN support (A = GCN1000L) and same sample after oxidative stabilization condition I (C = GCN1000LS) shift the temperature of maximum weight lost derivative, from 699 to 713°C. TGA results show thermal stability of the GCN1000 support increases with more aggressive oxidation treatment to remove amorphous carbon. T_{de} is shifted further for the harshest oxidation condition E is >750°C (beyond TGA experimental endpoint)..

TGA results are compared in Figure 3.18 with unmodified Ketjenblack carbon (BET surface area 835m^2 g^{-1}) which has T_{de} = 694.9°C. TKK Pt/C is made from similar high surface area carbon support, so Ketjenblack is representative of the carbon support used in TKK commercial catalyst. GCN weight loss due to stabilization is an order of magnitude smaller than Ketjenblack high surface area carbon at 750°C (1.6 vs. 18.0 wt. %) showing enhanced thermal stability of GCN -support material.

Increased thermal stability of the more graphitized GCN sample is in agreement with higher C-C bond energies 125 kcal mol^{-1} [34,35] for graphite relative to C-C single bond energies of 83-88 kcal mol^{-1} [36].

Platinum was deposited uniformly on the surface of the GCN1000 support. Pt/GCN sample was characterized using X-ray diffraction and Figure 3.2 compares 40% Pt/GCN with commercial TKK 46% Pt/C.

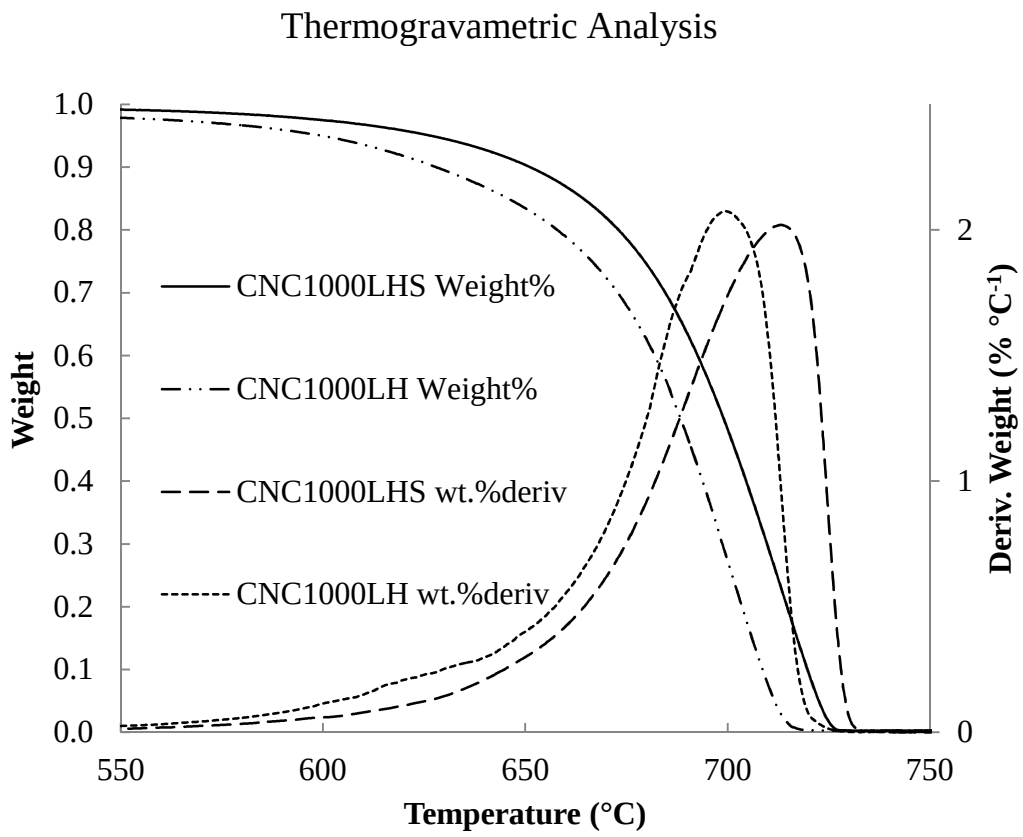

Figure 3.17 Thermal Stability is improved after stabilization by selective oxidation (GCN1000LHS) compared with same GCN without stabilization.

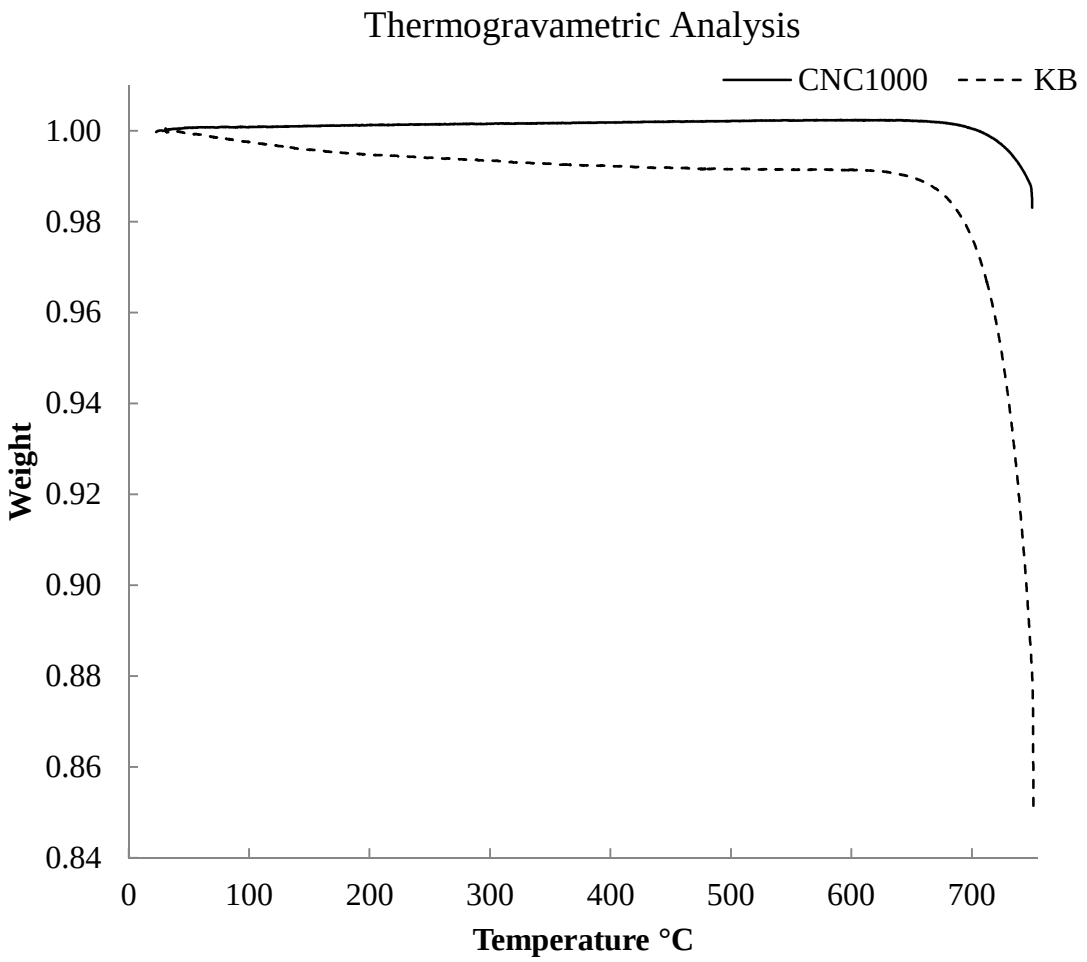

Figure 3.18 Enhanced thermal stability of GCN results in more than 50°C increase in thermal decomposition temperature, T_{de}, compared with Ketjenblack.

Platinum particle sizes were estimated to be 3.2nm by using Scherrer's equation applied to the X-ray diffraction patterns from Pt (2 2 0) crystal plane between 2Θ angles 60-75 [37]. TEM image in Figure 3.19 shows platinum deposition is well dispersed, with an average Pt particle size of 3.6nm, in agreement with XRD calculated particle size and the corresponding histogram is in Figure 3.20. ICP measured cobalt, and platinum loading amount in GCN1000 catalyst samples at 0.1 and 37.34% respectively for 40%Pt target loading.

3.6 Electrochemical Studies

3.6.1 Rotating ring-disk electrode (RRDE) studies

ORR activity was measured in oxygen saturated electrolyte to evaluate catalyst performance. Linear sweep voltammetry curve was also measured with nitrogen purged electrolyte after cleaning the catalyst surface by cycling between 0.05-1.10 V vs. RHE as a baseline for ORR activity without the double layer capacitance. Figure 3.21 shows the polarization curve for oxygen reduction of 40%Pt/ GCN1000, compared with 46%Pt/C TKK commercial catalyst. The measurement was performed with Pt loading of 20μg cm^{-2} using a potential scan rate of 5 mV s^{-1} and a rotation rate of 1600 rpm in a 0.1 M $HClO_4$ electrolyte solution saturated with O_2. The kinetic onset potential for ORR is similar for 40%Pt/ GCN (0.97 V) compared with 46%Pt/C TKK commercial catalyst (0.95 V), and the smaller diffusion current seen with the GCN1000 catalyst can be attributed to the lower surface area compared with TKK commercial catalyst (265 m^2 g^{-1} with Pt).

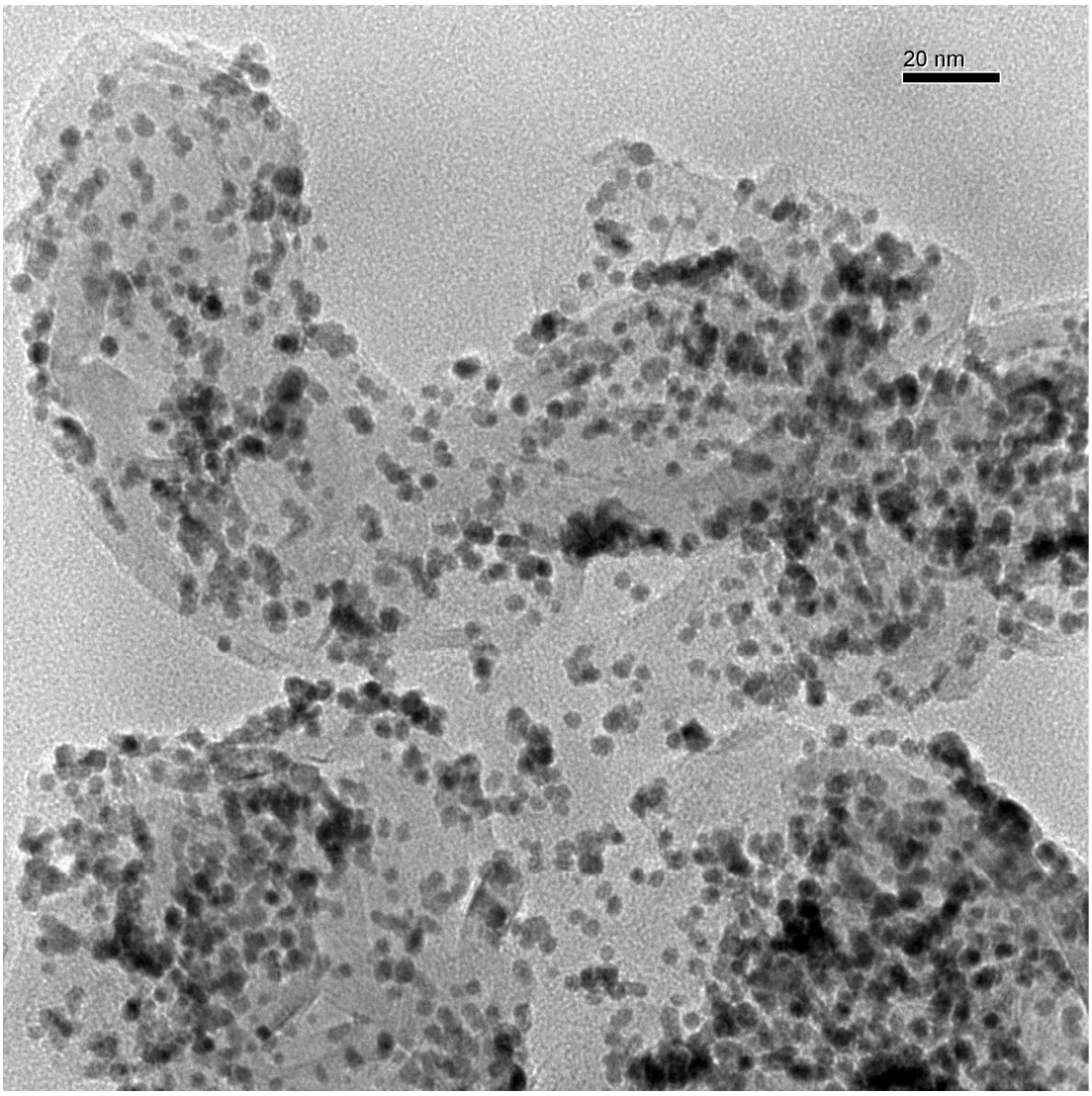

Figure 3.19 40wt. % Pt deposited on surface of the GCN1000 support.

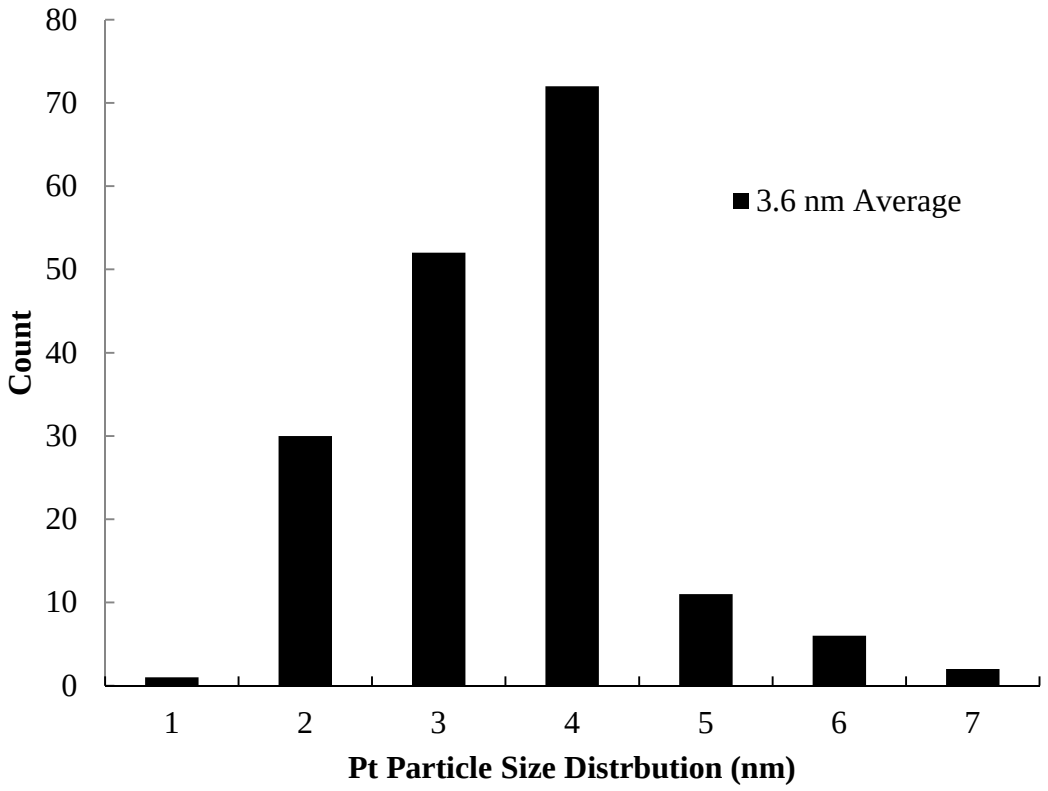

Figure 3.20 40%Pt/GCN 1000 Pt Particle Size Distribution.

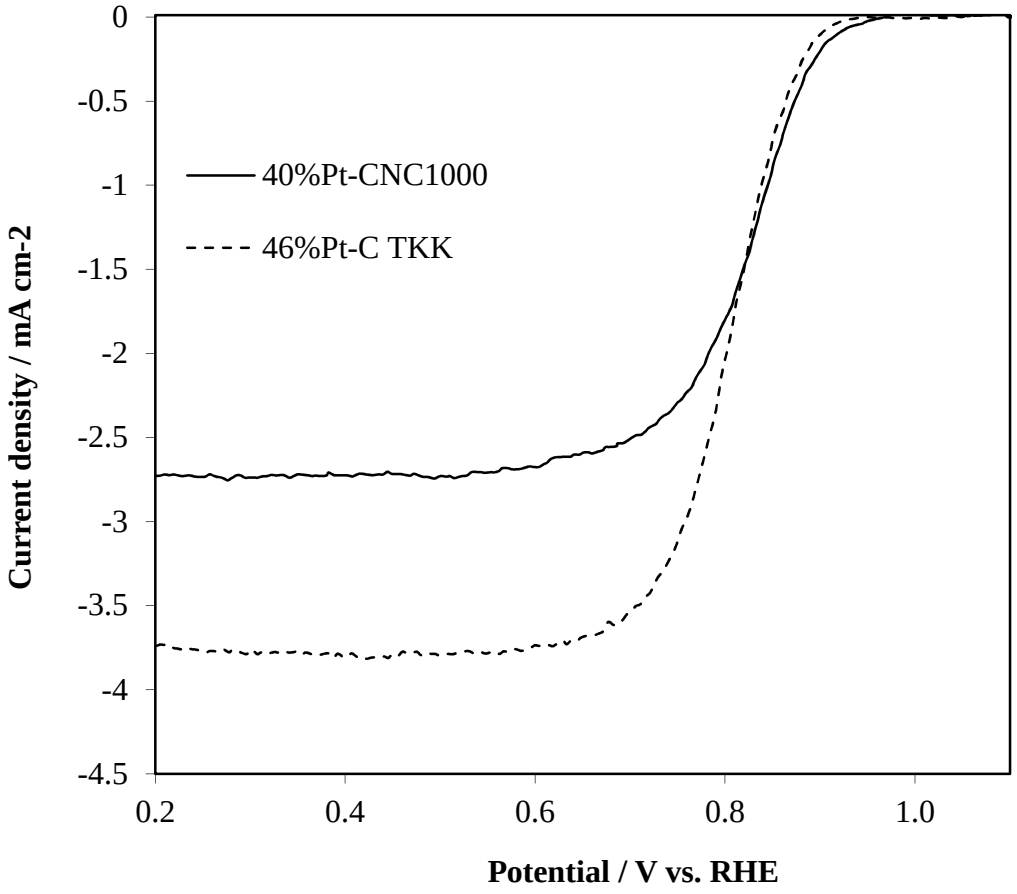

Figure 3.21 Fresh ORR activity of 40%Pt-GCN catalyst has similar kinetic onset potential as 46%Pt-C TKK commercial catalyst. Pt loading is 20µg cm^{-2} on glassy carbon electrode.

Catalyst stability was evaluated by periodically measuring ORR and ECSA after subjecting catalyst to N2 saturated potential cycling. Figure 3.22 shows the direct comparison of ORR activity for the 40%Pt/GCN catalyst before and after cycling 30,000 cycles 0.6-1.0V vs. RHE with very similar kinetic onset potentials to initial performance. 46%Pt/C TKK catalyst also shows good initial performance, however the potential cycling causes a large degradation (-44%) in current at 0.8 V vs. RHE. Contrasting the stable Pt/GCN results with the commercial catalyst in Figure 3.23 shows the electrochemical stability improvement. Peroxide formation varied from 1-3% for all catalysts tested for RRDE [38]. Electrochemically active surface area (ECSA) was determined using a conventional electrochemical method by integrating the area under the hydrogen desorption peak from 0.05 to 0.45 V vs. RHE, based on the electrical charge required for hydrogen desorption correlated with the (1 0 0) facets of the polycrystalline Pt Surface area (210 C cm^{-2}). [39,40] Electrochemical surface area shows significant improvement vs TKK commercial catalyst after cycling using Pt loading was 20µg cm^{-2} in Figure 3.24. The GCN supported platinum catalyst shows 10% less change in electrochemical surface area (ECSA) after cycling 5,000 between 0.6 – 1.0V vs RHE as compared with Pt/C Commercial Catalyst. The ECSA of Pt/GCN catalyst plateaus after 20,000 cycles, and shows 25% less change in ECSA compared with the same commercial catalyst. Pt/GCN electrochemical surface area decreases 31% from 42.59 to 29.39 m^2 g^{-1} Pt after 30,000 cycles between 0.6 and 1.0V vs. RHE. This compares favorably with commercial TKK 45.8% Pt/C catalyst which decreases 56% ECSA from 90.35 to 39.53 m^2 g^{-1}. The Pt/GCN support shows less %ECSA loss in 30,000 cycles than the commercial catalyst loses after only 5,000 cycles.

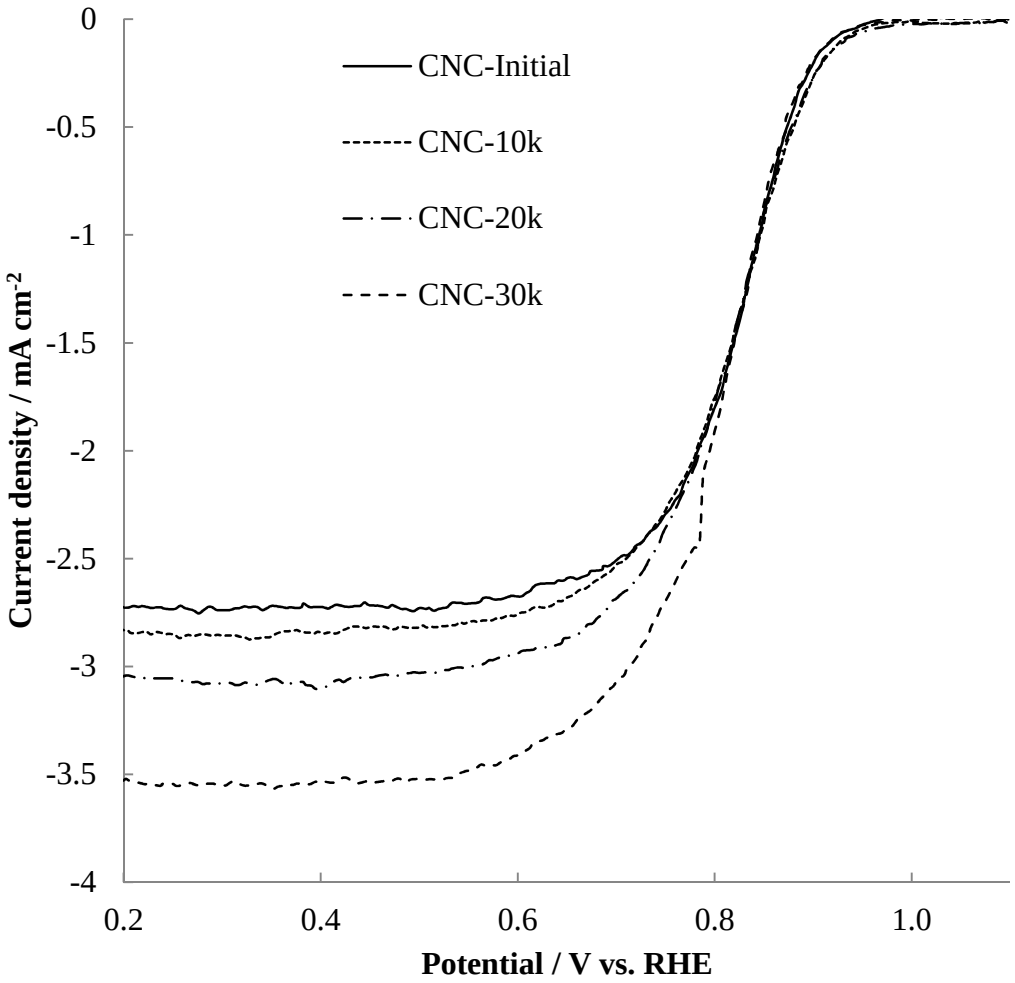

Figure 3.22 40Pt/GCN ORR cycling shows very stable kinetic onset potential as a function of electrochemical potential cycling. Pt loading 20µg cm^{-2} was deposited on the glassy carbon electrode.

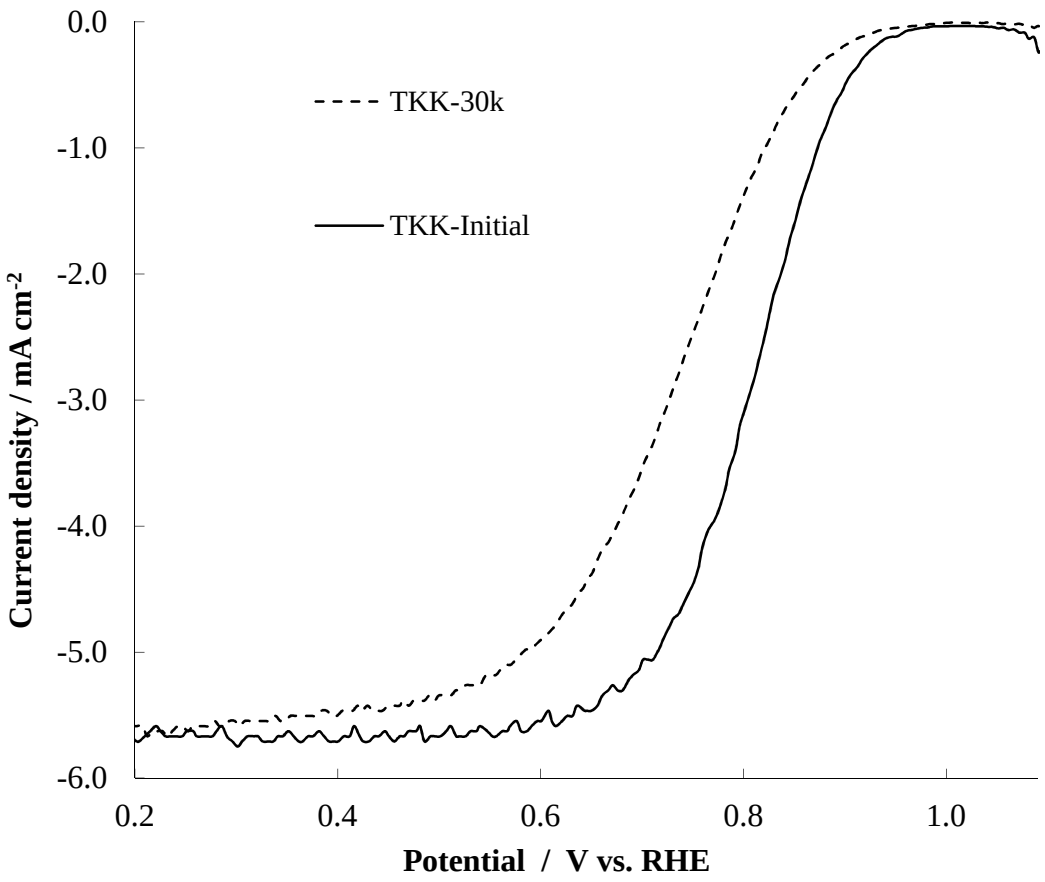

Figure 3.23 46Pt/C TKK ORR cycling results in degraded kinetic onset potential after electrochemical cycling. Pt loading 100 µg cm^{-2} was deposited on the glassy carbon electrode.

Table 3.3 ORR Kinetic onset current before and after electrochemical cycling in N_2.

Electrochemical cycling in N_2 (0.6-1.0 V) Cycle#	40%Pt / GCN1000 ORR Current mA cm^{-2} @ 0.8V	46%Pt / TKK Commercial ORR Current mA cm^{-2} @ 0.8V
Initial	-1.795 (1.00x)	-3.10716 (1.00x)
10k	-1.751	
20k	-1.769	
30k	-1.905 (1.06x)	-1.3734 (0.56x)
Catalyst loading (µg Pt cm^{-2})	20	100

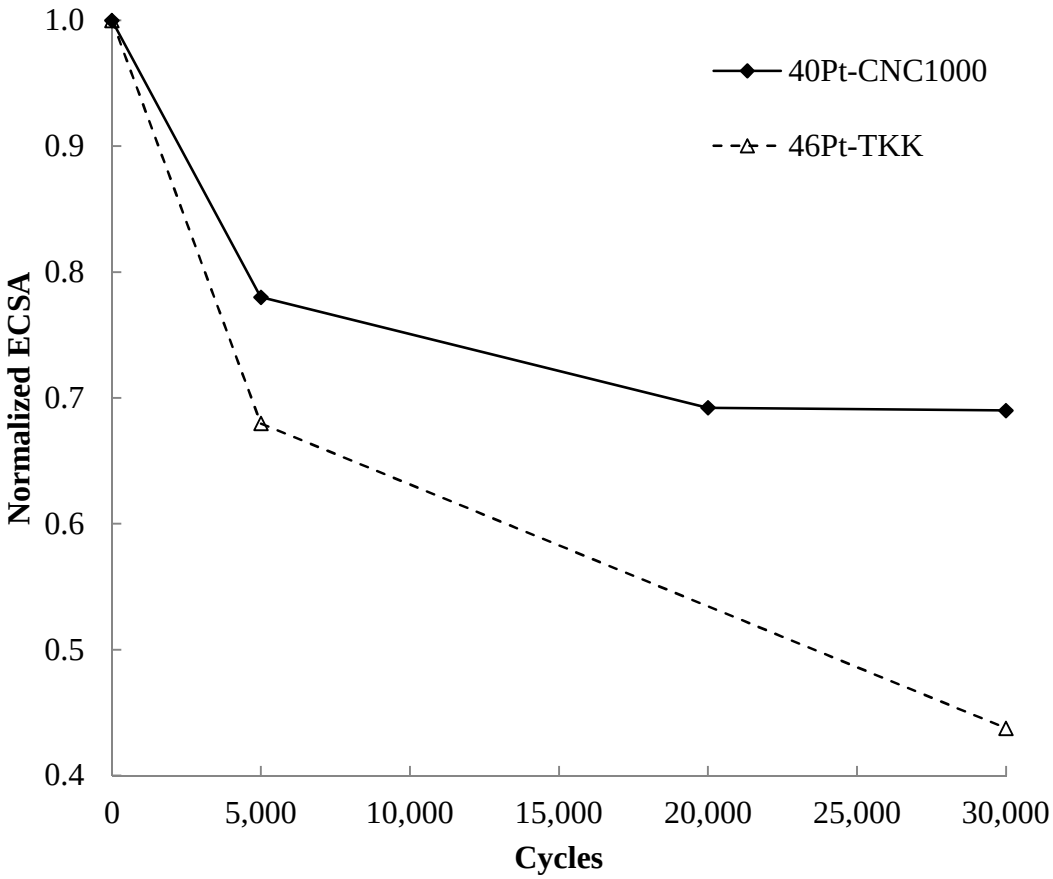

Figure 3.24 ECSA as function of cycle number (0.6V – 1.0V) shows improved stability for GCN-supported catalyst compared with Pt/C TKK commercial catalyst.

The improvement in electrochemical stability presented here can be attributed to removal of unstable amorphous carbon prior to Pt deposition on the GCNs in addition to surface accessible porous structure of the underlying graphitic support. The superior cycling stability is due to better Pt catalyst-GCN support interaction when compared to commercial high surface area carbon (Ketjen black -835 m2 g^{-1}) supported catalyst. Commercial TKK 46%Pt/C catalyst uses Ketjen black carbon with high amount of amorphous carbon, and support-catalyst interaction is not good in TKK commercial catalyst, but is better in GCN. The electrochemical difference may also be due to the highly graphitized Pt/GCN catalyst structure. Amorphous carbon impurities in carbon nanotubes have been reported to have a strong negative impact on electrochemical performance as measured by cyclic voltammetry [21], so the selective oxidative removal of these amorphous impurities also should be contributing factor in ECSA half-cell stability improvements.

The main mechanisms for loss of catalytic activity are Pt dissolution, Oswald ripening of Pt particles, and agglomeration coalescence of nanoparticles by collision or movement on carbon support [39,41,42,43,44]. The large surface accessible pores may be a favorable morphology against platinum agglomeration or dissolution.

3.6.2 Fuel Cell Performance

The Pt/GCN catalyst was prepared into a MEA to test performance in Fuel Cell in H_2-O_2, H_2-Air and in-situ ECSA measurements. H_2-O_2 current density of Pt/GCN catalyst is 1934 mA cm^{-2} at 0.7 $V_{iR\text{-}free}$ is improved compared to Pt/C commercial TKK of 1913 mA cm^{-2} at 0.7 $V_{iR\text{-}free}$, in Figure 3.25.

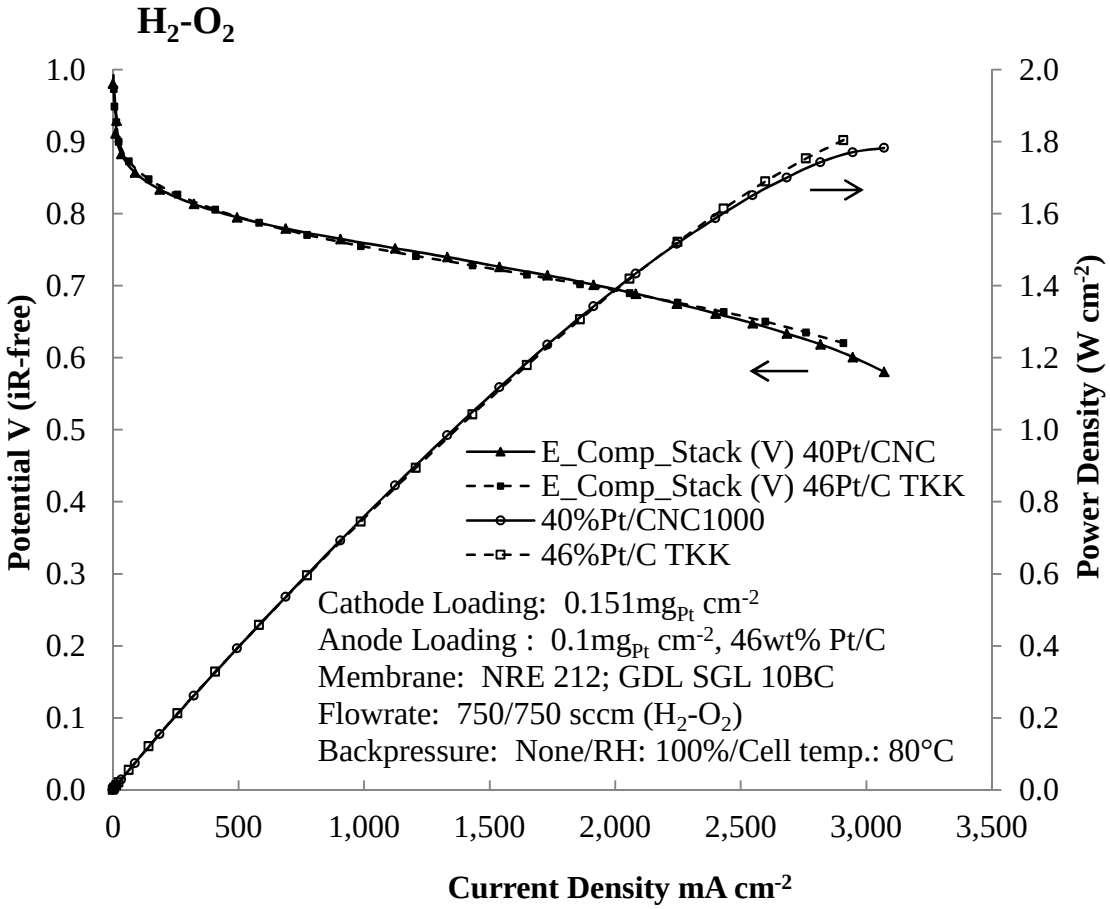

Figure 3.25 H_2-O_2 MEA fuel cell testing of 40Pt/GCN1000 vs 46Pt/C TKK commercial catalyst.

H_2-Air current density of Pt/GCN catalyst is 932 mA cm^{-2} measured at 0.6 $V_{iR\text{-}free}$ is improved compared to Pt/C commercial TKK of 859 mA cm^{-2} at 0.6 $V_{iR\text{-}free}$. Power density is also higher for the Pt/GCN in the mass transport limited region under larger current density loading compared with the TKK commercial catalyst, due in part to reduced iR-loss in the Pt/GCN catalyst. Power density at lower voltages is important for automotive applications of fuel cell catalysts. The increased power of the Pt/GCN catalyst with H_2-Air is shown in Figure 3.26. The polarization curves demonstrated good ORR kinetics and fuel cell performance for Pt/GCN catalyst synthesized at USC. GCN1000 Mass activity is 0.143 A mg^{-1} Pt at 0.9$V_{iR\text{-}free}$. This activity is similar to reported literature values of 0.104 – 0.16 A mg^{-1} Pt at 0.9$V_{iR\text{-}free}$ for 46% Pt/C TKK commercial catalyst [45,46].

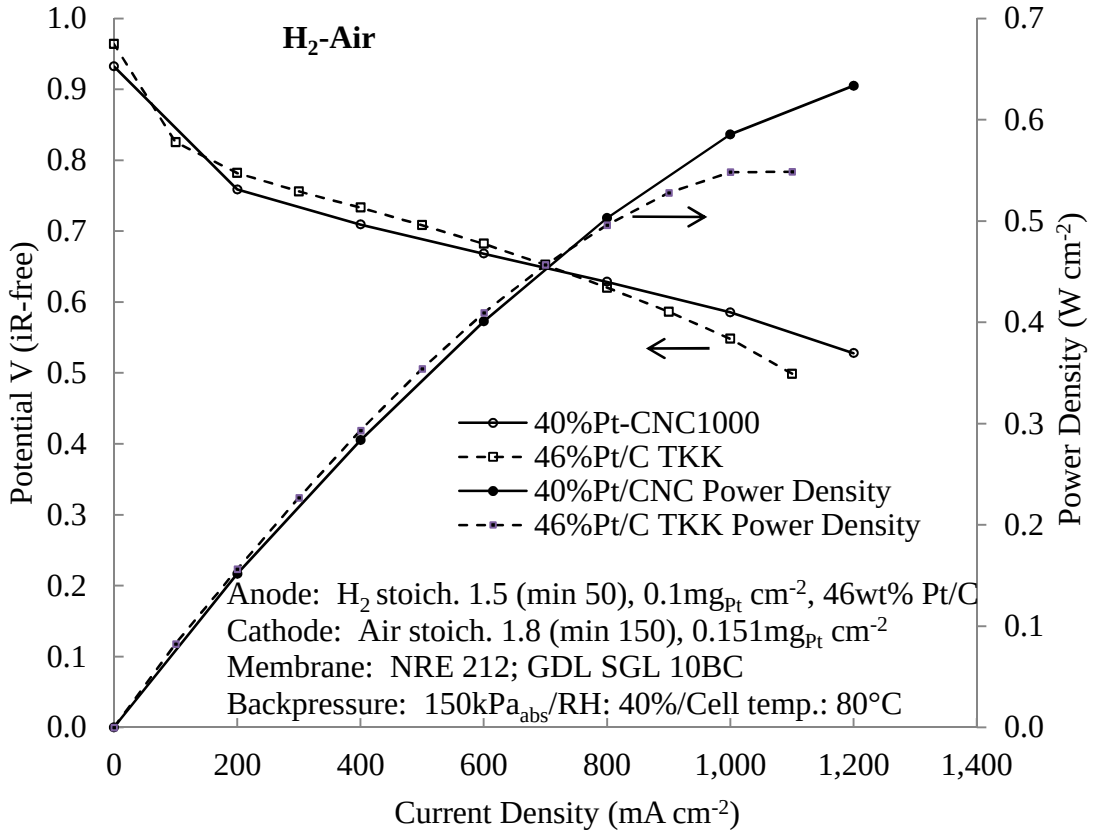

Figure 3.26 H_2-Air MEA fuel cell performance 40Pt/GCN power density is higher compared with 46%Pt/C TKK commercial catalyst at high current density in the mass transport region.

CHAPTER 4

CONCLUSION

This work presents a simple method for preparation of hollow graphitic carbon nanostructures with ~50-100 nm diameter and ~10 nm wall thickness. These GCNs have a porous structure which is surface accessible, not framework confined pores. Solid phase synthesis followed by selective oxidative removal of unstable amorphous carbon presents a unique stable support system with tunable pore size and BET surface area to achieve desired catalyst performance.

The highly crystalline graphitic nature of this novel catalyst support preparation results in improved stability. The thermal stability as measured by TGA weight loss is an order of magnitude more stable compared with high-surface area Ketjenblack carbon. Catalyst stability improvement is due to better catalyst-support interaction and the removal of amorphous carbon. Pt/GCN shows improved electrochemical stability of the carbon support measured by CV after 30,000 cycles in RRDE half-cell experiments.

This catalyst shows good performance for oxygen reduction reaction in PEM Fuel Cell, with increased power density in the mass transport region compared to commercial TKK catalyst.

This approach of controlling the strength of the selective-oxidation condition can be applied generally, however optimal stabilization conditions are dependent on support properties such as metal content and degree of graphitization. The precise stabilization conditions will vary for different catalyst supports, requiring support-specific optimization to effectively utilize this stabilization method to improve catalyst support stability.

The financial support of DOE under grant DE-EE0000460 is gratefully acknowledged.

REFERENCES

[1] C.-K. Tsai, H.Y. Kang, C.-I. Hong, C.-H. Huang, F.-C. Chang, H. Paul Wang, J. Nanopart. Res. 14 (2012) 1315

[2] X.S Zhao, F. Su, Q. Yan, W. Guo, X. Y. Bao, L. Lv, Z. Zhou, J. Mater. Chem.16 (2006) 637-648

[3] H. Yang, D. Zhao, J. Mater. Chem. 15 (2005) 1217-1231

[4] K. Y. Chan, J. Ding, J. Ren, S. Cheng, K.Y. Tsang, J. Mater. Chem. 14 (2004) 505-516

[5] D.S. Bethune, C.H. Klang, M.S. de Vries, G. Gorman, R. Savoy, J. Vazquez, R. Beyers, Nature 363 (1993) 605

[6] F. J. Derbyshire, A.E.B. Presland, D.L. Trimm, Carbon 13(1975) 111

[7] H. Marsh, Pure Appl. Chem. 20 (1970) 133

[8] A. Oya, S. Otani; Carbon 17 (1979) 131 DOI: 10.1016/0008-6223(79)90020-4

[9] A. Oya, H. Marsh, J. Mater. Sci. 17-2 (1982) 309-322

[10] N.I. Maksimova, O.P. Krivoruchko, G. Mestl, V.I. Zaikovski, A. L. Chuvilin, E.B. Burgina, J. Mol. Catal. A: Chem. 158 (2000) 301-307.

[11] T. Hyeon, S. Han, Y.-E. Sung, K.-W. Park, Y.-W. Kim, Angew, Chem. Int. Ed. 42 (2003) 4352-4356.

[12] M. Sevilla, C. Sanchis, T. Valdes-Solis, E. Morallon, A.B. Fuertes, J. Phys. Chem. C 111 (2007) 9749-9756.

[13] S.-Y. Huang, P. Ganesan, S. Park, B.N. Popov, J. Am. Chem. Soc. 131 (2009) 13898-13899.

[14] H.–S. Oh, K.H. Lim, B. Roh, I. Hwang, H. Kim, Electrochimica Acta, 54 (2009) 6515-6521.

[15] N. Fujiwara, K. Yasuda, T. Ioroi, Z. Siroma, Y. Miyazaki, Electrochimica Acta 47 (2002) 4079-4084.

[16] X. Li, H.R. Colon-Mercado, G. Wu, J.-W. Lee, B.N. Popov, Electrochemical and Solid-State Letters 10-11 (2007) B201-B205.

[17] H. Liu, J. Li, F. Wang, J. Liu, J. Ji, Electrochimica Acta 93 (2013) 25-31.

[18] M. Sevilla, A.B. Fuertes, Carbon 44 (2006) 468-474.

[19] H. Marsh, D. Crawford, D.W. Taylor, Carbon 21-1 (1983) 81-87.

[20] M. Sevilla, C.S. Matinez-de Lecea, T. Valdes-Solis, E. Morallon, A.B. Fuertes, Phys. Chem. Chem. Phys. 10 (2008) 1433-1442.

[21] A. Ambrosi, M. Pumera, J. Phys. Chem. C 115 (2011) 25281-25284.

[22] J. -F. Colomer, P. Piedigrosso, A. Fonseca, J.B. Nagy, Sunthetic Metals 103 (1999) 2482-2483.

[23] P.-X. Hou, C. Liu, H.-M. Cheng, Carbon 46 (2008) 2003-2025.

[24] V.T. Le, C.L. Ngo, Q.T. Le, T.T. Ngo, D.N. Nguyen, M.T. Vu, Adv. Nat. Sci. Nanosci. Nanotechnol. 4 (2013) 035017.

[25] R. Verdejo, S. Lamoriniere, B. Cottam, A. Bismarck, M. Shaffer, Chemical Communications 43- 5 (2007) 513-515.

[26] I.W. Chiang, B.E. Brinson, R.E. Smalley, J.L. Margrave, R.H. Hauge, J. Phys. Chem. B 105 (2001) 1157-1161.

[27] S.C. Tsang, P.J.F. Harris, M.L.H. Green, Nature 362 (1993) 520-522.

[28] B. Fei, H. Lu, Z. Hu, J.H. Xin, Nanotechnology 17 (2006) 1589-1593.

[29] Z. Liu, X. Lin, J.Y. Lee, W. Zhang, M. Han, L.M. Gan, Langmuir 18 (2002) 4054-4060.

[30] H. Hu, B Zhao, M.E. Itkis, R.C. Haddon, J. Phys. Chem. B 107 (2003) 13898-13842.

[31] M. Kruk, V. Antochshuk, J.R. Matos, L.P. Mercuri, M. Jaroniec, J. Am. Chem. Soc. 124 (2002) 768-769.

[32] A.H. Janssen, A.J. Koster, K.P. de Jong, J. Phys. Chem. B 106 (2002) 11905-11909.

[33] S. Naumov, “Hysterysis Phenomena in Mesoporous Materials,” , University of Leipzig, Dissertation, 2009

[34] R. Heyrovska (2008) Various Carbon to Carbon Bond Lengths Inter-related via the Golden Ratio, and their Linear Dependence on Bond Energies. [Online], “Available: arXiV:0809.1957v1[physics.gen-ph],” [Online]

[35] Hugh O. Pierson, Handbook of Carbon, Graphte, Diamond, and Fullerenes: Properties, Processing, and application: William Andrew Inc., 1993

[36] L. Pauling, The Nature of the Chemical Bond, NY: Cornell Univ. Press, 1960

[37] S.-Y. Huang, P. Ganesan, B. Popov, Applied Catalysis B: Environmental 93 (2009) 75-81.

[38] V. Nallathambi, J.-W. Lee, S.P. Kumaraguru, G. Wu, B.N. Popov, J. Power Sources 183 (2008) 34-42.

[39] H. Colon-Mercado, B.N. Popov, J. Power Sources 155 (2006) 253-263.

[40] H. A. Gasteiger, G. D. Stab, P. M. Urban, D. M. Kolb, R.J. Behm, T. J. Schmidt, J. Electrochem. Soc. 145-7(1998) 2354-2358.

[41] S Chen, W. Sheng, N. Yabuuchi, P.J. Ferreira, L.F. Allard, Y. Shao-Horn, J. Phys. Chem. C 113 (2009) 1109-1125.

[42] P. Yu, M. Pemberton, P. Plasse, J. Power Sources 144 (2005) 11-20

[43] T.F. Fuller, ECS Trans 1 (2006) 345-353.

[44] P.J. Ferreira, J. Electrochem. Soc 152-11 (2005) A2256-A2271.

[45] P. Mani, R. Srivastava, P. Strasser, J. Phys. Chem. C 112 (2008) 2770-2778.

[46] H.A. Gasteiger, S.S. Kocha, B. Sompalli, F.T. Wagner, Allied Catalysis B: Environmental 56 (2005) 9-35.